Alma Mater Studiorum · University of Bologna

School of Science
Department of Physics and Astronomy
Master Degree in Physics

Study of the impact of out-of-target fragmentation in cross section measurements with the FOOT experiment

Supervisor:
Prof. Matteo Franchini

Co-supervisors:
Dr. Roberto Zarrella
Dr. Giacomo Ubaldi

Submitted by:
Francesco Vascelli

Academic Year 2021/2022

Abstract

Hadrontherapy is an innovative cancer treatment technique that utilizes beams of charged particles, specifically protons and heavier ions, to target tumors deep within the body. These particles have a unique depth-dose distribution in tissue, with low doses at the entry point and a sharp peak of maximum dose (known as the Bragg peak) near the end of their path. This makes them effective at targeting tumors while minimizing damage to surrounding healthy tissues. Carbon and oxygen ions, in particular, have been found to have an enhanced biological effect, making them useful for treating radioresistant tumors. However, it is important to consider nuclear interactions in these treatments. As beam particles travel through the body, they can fragment and release a non-zero dose beyond the Bragg peak. Additionally, fragments of nuclei present in the human body can modify the dose released in healthy tissues. The lack of comprehensive data on cross sections makes it difficult to predict the effects of these interactions. To fill these gaps in experimental data, the FOOT experiment has been designed to detect, track and identify charged fragments produced in ion collisions with different targets. Its final goal is to measure double differential cross sections both in angle and kinetic energy with an uncertainty lower than 5%. However, cross section measurements can be spoiled by out-of-target fragmentations that could occur anywhere along the experimental apparatus, such as in the detectors' planes or in the air surrounding them. In this thesis, a straightforward algorithm for event classification, based on the zone of fragmentation, is presented and studied. First, the accuracy of the classification is analyzed to ensure the proper functioning of the algorithm. Then, the effectiveness of a selection on events, based on the classification algorithm, is evaluated through the study of reconstructed tracks. To do so, a sample of simulated data of ^{16}O at 400 MeV/n impinging on a target of graphite is employed.

Contents

Introduction

Cancer is one of the most widespread health problems and a leading cause of death worldwide, accounting for almost 10 million deaths in 2020, according to World Health Organization (WHO).

Cancer, also known as tumor, refers to a diverse group of diseases that can develop in any part of the body. The hallmark of cancer is the rapid growth of abnormal cells that surpass their normal boundaries, invade neighboring tissues, and potentially spread to other organs in the body. Various cancer types necessitate specific treatment strategies that may involve one or multiple approaches such as surgery, chemotherapy, radiotherapy, and immunotherapy. However, recent technological advancements have led to the emergence of a novel radiation therapy technique as an alternative to conventional radiotherapy, known as hadrontherapy, which utilizes charged particle beams.

Hadrontherapy is an innovative cancer treatment modality that exploits the unique energy deposition mechanism associated with the interaction of charged hadrons, such as protons and other ions, with matter. Unlike photons or electrons, hadrons deposit most of their energy near the end of their path, resulting in the creation of a peak in energy deposition, known as the Bragg peak, at a specific depth within the target tissue. This feature allows for the delivery of a higher radiation dose to the tumor while minimizing the collateral damage to the surrounding healthy tissues and organs at risk. However, hadrontherapy beams may produce nuclear fragmentation that leads to a distortion in the dose deposition profile

Indeed, when beams interact with nuclei within the human body, they can generate two types of fragments. The first type, known as projectile fragments, consists of high-energy particles that can cause dose deposition beyond the Bragg peak. The second type, called target fragments, has low momentum and deposits its energy near the site of generation, leading to dose deposition in healthy tissues before the Bragg peak. These processes can have significant effects on the outcome of hadrontherapy treatments, and thus require detailed investigation due to the current lack of experimental data and precise models on it.

The FOOT (FragmentatiOn Of Target) experiment aims to fill this gap by measuring the cross sections of both target and projectile fragmentation that are relevant for hadrontherapy using beams and targets of protons, carbon and oxygen ions, the most

common elements in the human body and, at the same time, the most used therapy beam types. In order to achieve this goal, the experiment will perform measurements in both direct and inverse kinematic approach to overcome the challenges associated with the short range of the generated fragments (on the order of micrometers). Additionally, to address the difficulties in managing a pure hydrogen target, the data is obtained by subtracting the cross-sections measured on carbon (C) and polyethylene (C_2H_4) targets. The same approach is used for oxygen, which is studied using a polymethyl methacrylate (PMMA, $C_5O_2H_8$) target.

The aim of this thesis is the study of the effect of out-of-target fragmentation in the FOOT experiment. Indeed, fragmentation could happen not only inside the target, but also on detectors or the air surrounding them. This could spoil the cross section measurement, so they need to be removed in the analysis process. To do so, a straightforward algorithm for event classification was developed and studied, using simulated data based on the apparatus employed in the data taking campaign that took place at GSI laboratories in July 2021, where a beam of ^{16}O at 400 MeV/n impinging on a target of graphite was employed.

In Chapter 1, an overview of charged particles interactions with matter, with a focus on hadrontherapy and radiobiology is presented. In Chapter 2, the FOOT experiment is introduced, illustrating its purposes and the characteristics of each subdetector in the electronic setup. In Chapter 3, the procedure is described, including details on the GSI2021 campaign and FOOT analysis software, SHOE. In Chapter 4, the results of the classification algorithm are reported.

Chapter 1

Charged particles interaction with matter

Heavy charged particles undergo many different interactions as they traverse matter. The main process is *Coulomb scattering*, an electromagnetic interaction with the orbital electrons of the atoms of the medium. While having smaller probability to occur, *nuclear interaction* is also of critical importance, considering its applications in particle therapy. In this chapter an introduction to both electromagnetic and nuclear interactions is presented, focusing on the aspects that will become meaningful in hadrontherapy.

1.1 Electromagnetic interaction

As a charged particle interacts with the electrons of the absorbing medium, energy is transferred. From the relativistic two-body scattering calculation, the maximum energy transferred in a single collision is a small fraction of the total energy of the charged particle [1]. As such, before losing all its energy the particle will interact many times, in a quasi-continuous process. It is then possible to define a so called *stopping power* S as the energy loss per unit length:

$$S = -\frac{\mathrm{d}E}{\mathrm{d}x} \tag{1.1}$$

This quantity was first calculated by Bohr using classical arguments and three important assumptions: firstly, it is assumed that the electron is free and initially at rest (i.e. its orbital velocity must be much lower than the ion velocity). Secondly, it is assumed that the electron only moves very slightly during the interaction with the heavy particle so that the electric field acting on it may be taken at its initial position. Lastly, it is supposed that the incident particle remains essentially undeviated from its original path because of its much larger mass $M_{particle} >> m_{electron}$.

1.1.1 The Bethe-Bloch formula

The stopping power was later revised by Bethe and Bloch [2] using quantum mechanics. The resulting Bethe-Bloch formula for mean stopping power is:

$$-\left\langle \frac{\mathrm{d}E}{\mathrm{d}x} \right\rangle = 4\pi N_A r_e^2 m_e c^2 \frac{Z\rho}{A} \frac{z^2}{\beta^2} \left[ln \frac{2m_e c^2 \beta^2 \gamma^2}{I} - \beta^2 - \frac{\delta(\gamma)}{2} - \frac{C}{Z} \right] \tag{1.2}$$

where N_A is the Avogadro Number, r_e and m_e are respectively the classical radius and the mass at rest of the electron and c is the speed of light; Z, A and ρ are respectively the atomic number, the mass number and the density of the target; z, β and γ are respectively the atomic number, the velocity and the Lorentz factor of the charged particle; I is the mean ionization energy of the target and δ and C are correction factors.

Highlighting the dependence on the medium, it is mostly due to the density ρ. In fact, $\frac{Z}{A}$ is roughly 0.5 for most light stable elements and the mean excitation potential I contributes logarithmically. To incorporate the dependency on the density, it is useful to introduce the *mass stopping power* of a material, defined as:

$$\frac{\mathrm{d}E}{\mathrm{d}\chi} \equiv \frac{1}{\rho} \frac{\mathrm{d}E}{\mathrm{d}x} \tag{1.3}$$

where χ is the mass thickness of the material in units of $\frac{g}{cm^2}$. In this way, the stopping power would be roughly the same for very different kinds of mediums, which is also more convenient when dealing with mixed materials.

The main feature of the Bethe-Bloch formula is the dependency of the stopping power on the particle velocity β and its charge z. At lower energies, the $\frac{1}{\beta^2}$ factor dominates, and the stopping power decreases until a minimum around $\beta\gamma = 3$; as the energy increases, the $ln(\beta^2)$ term dominates so a logarithmic rise is found. This behaviour can be seen in Fig. 1.1. On the other hand, the mass stopping power depends on the square of the particle charge and not on its mass. This means that different ions would lose different amount of energy, as seen in Fig. 1.2

1.1.2 Bethe-Bloch corrections

The Bethe-Bloch equation (Eq. 1.2) is valid only if $0.05 < \beta\gamma < 500$ and for particles heavier than the muon. At low velocities the charge of the particle decreases due to ionization and recombination processes [4] and it has to be replaced with an effective charge z_{eff} which can be modeled as:

$$z_{eff} = z(1 - e^{-125\beta z^{-2/3}}) \tag{1.4}$$

Still, even at low velocities the assumption that the atomic electron is at rest is not true and so the *shell correction* holds ($\frac{C}{Z}$ term). At high energies, the *density term* δ term

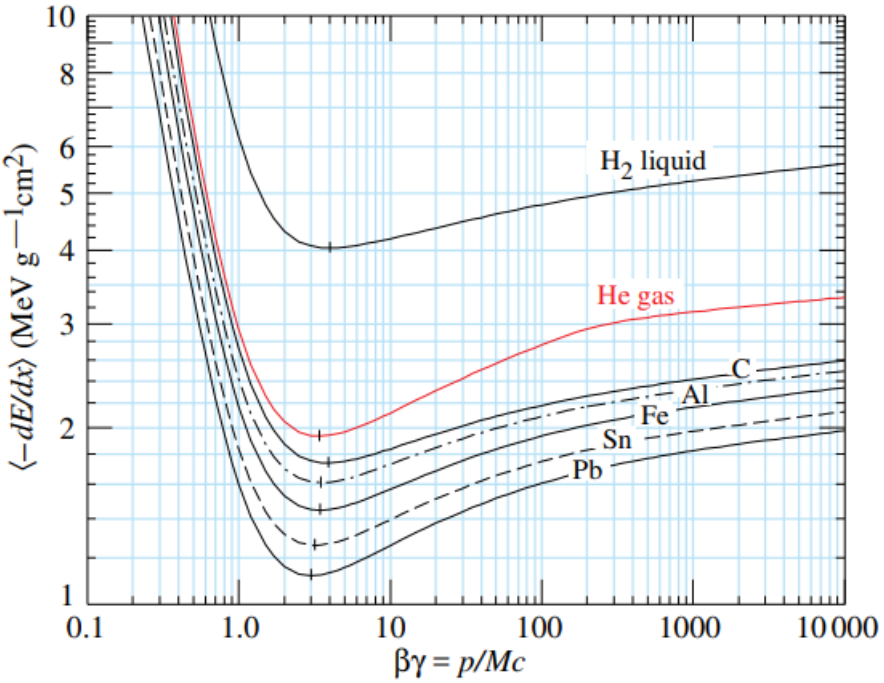

Figure 1.1: Mean mass stopping power versus $\beta\gamma$ for particles with $z = 1$ in different materials [3].

becomes important: as a consequence of increased electric field, the atoms close to the path of the particle start to polarize resulting in a reduction of the force exerted on far electrons. This effect is stronger for dense material with respect to lighter materials, such as gases.

1.1.3 Range and energy-loss fluctuations

The behaviour of heavy charged particle in matter allows to define a *range* R, as the distance traveled by a particle before losing all of its energy:

$$R = \int_0^{E_{k_i}} \left(\frac{\mathrm{d}E}{\mathrm{d}x}\right)^{-1} \mathrm{d}E \tag{1.5}$$

where E_{k_i} is the initial kinetic energy of the particle. However, a set of identical particles with the same initial velocity do not stop at the same depth, even if the energy-loss process is continuous. Fluctuations in path length of particles are present due to the statistical nature of the collision process. This phenomenon is called *range straggling* and it is due to the fluctuations in the energy-loss [5]. They are described by the Vavilov distribution which can be approximated to a Gaussian distribution in the limit of many

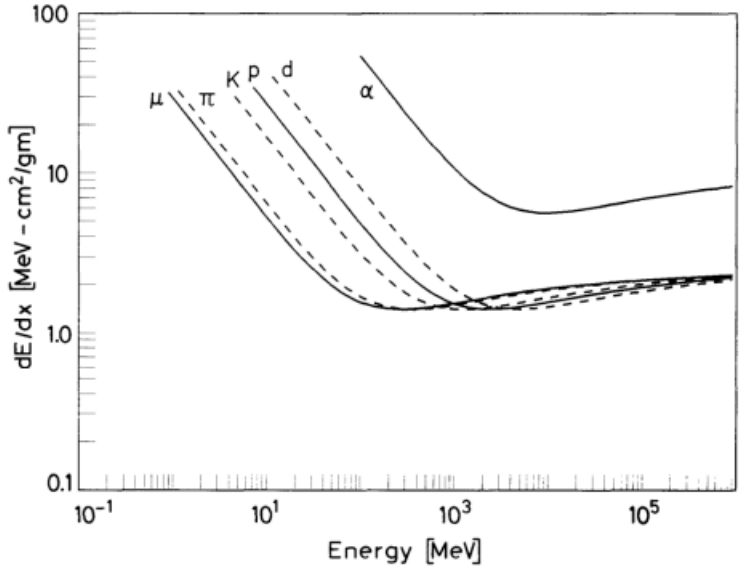

Figure 1.2: Mass stopping power versus energy for different charged particles. The alpha particle ($z = 2$) loses roughly 4 times more energy than other charged particles (all having $z = 1$).

collisions as stated by the central limit theorem:

$$f(\Delta E) = \frac{1}{\sqrt{2\pi\sigma^2_{\Delta E}}} \exp\left[\frac{(\Delta E - \overline{\Delta E})^2}{-2\sigma^2_{\Delta E}}\right] \tag{1.6}$$

The range straggling σ_R is directly related to the energy straggling by the equation:

$$\sigma^2_R = \int_0^{E_{k_i}} \left(\frac{\mathrm{d}\sigma^2_{\Delta E}}{\mathrm{d}x}\right) \left(\frac{\mathrm{d}E}{\mathrm{d}x}\right)^{-3} \mathrm{d}E \tag{1.7}$$

and the relative range straggling can be written as:

$$\frac{\sigma_R}{R} = \frac{1}{\sqrt{m}} f(\gamma) \tag{1.8}$$

where f is a slowly varying empirical function depending on the absorber and γ is the Lorentz factor for the incident particle. It is evident that range fluctuations are greater for lighter nuclei.

1.2 Nuclear interactions

Although electromagnetic interactions are the main contributors to energy loss in matter, it is impossible to neglect the contribution of nuclear interactions, as their effects are of great importance in hadrontherapy.

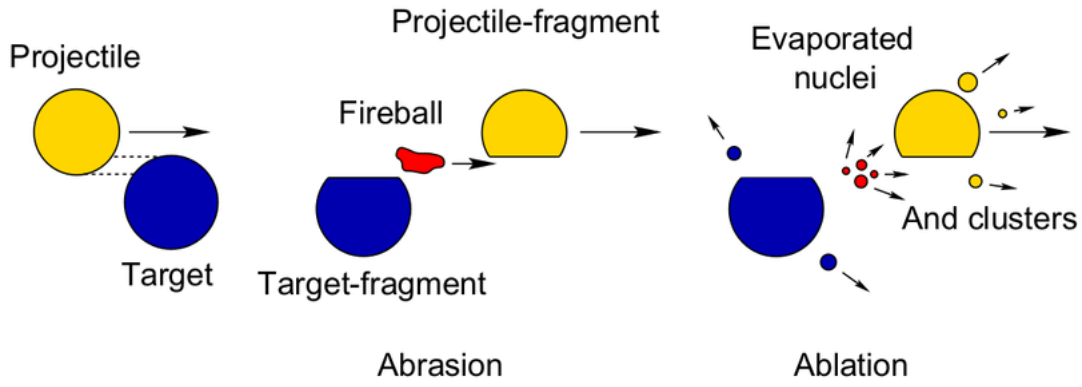

Figure 1.3: A schematic view of the abrasion-ablation model [7].

Nuclear interactions are charge-independent short range interactions between nucleons with enough energy to overcome the Coulomb barrier. For the purpose of this thesis, only *inelastic nuclear collisions*, where new particles are produced as a consequence of nuclear structure changes, are considered.

1.2.1 Abrasion-ablation model

The most frequently occurring nuclear reactions are peripheral collisions where the beam particles may lose one or several nucleons. This process can be described by the *abrasion–ablation model* [6] as illustrated in Fig. 1.3. Nucleons in the overlapping zone between the interacting projectile and the target nucleus are "abraded" and form a hot reaction zone (fireball), whereas the outer nucleons (spectators) are only slightly affected by the collision. The fireball is treated relativistically as an ideal gas whose temperature is determined by the available energy per nucleon.

In the second step (ablation), the remaining projectile and target fragments as well as the fireball de-excite by evaporating nucleons and light clusters. Those emitted from the projectile fragments appear forward peaked in the laboratory frame due to the high initial velocity of the projectile. The projectile fragments continue travelling with nearly the same velocity and direction as the projectile itself. Neutrons and clusters from target fragments are emitted isotropically and with much lower velocities. Nuclear fragmentation reactions lead to an attenuation of the primary beam flux and a build-up of lower-Z fragments with increasing penetration depth. The lower-Z fragments have longer ranges than the primary ions as the range of particles (at the same velocity) scales with A/Z^2.

1.2.2 Nuclear cross section

The *cross section* is a physical quantity that can be used to describe the probability for a particular reaction to occur [8]. Let's suppose that a uniform beam of N_0 particles with velocity v impinges on a target of area S and differential thickness dx. The incoming flux is:

$$\phi_0 = n_0 \cdot v$$

where $n_0 = N_0/V$ is the particle density of the beam. Instead, the particle density of the target is defined as:

$$n_t = \frac{N_A \rho}{A_t}$$

where N_A is the Avogadro number, ρ is the target mass density and A_t is the target mass number. During the crossing of the target, some particles from the beam may interact with the particles of the target. The number of particles that interact per unit of time is then:

$$\frac{\mathrm{d}N}{\mathrm{d}t} = \phi_0 \; n_t \; \sigma_R \; dV \tag{1.9}$$

where $dV = S \cdot dx$ is the target infinitesimal volume. The proportionality term σ_R is the cross section. It has the dimension of an area and it is measured in *barns* ($1\ b = 10^{-24}\ cm^2$), so it can be considered as the surface of the superposition between the projectile and the target.

The measurement of a certain interaction can be described also in terms of different parameters, such as the kinetic energy or the scattering angle of the produced fragment. So we can define new quantities, such as the *differential cross section* or even the *double differential cross section*:

- differential cross section in solid angle $\frac{d\sigma_R}{d\Omega}$
- differential cross section in energy $\frac{d\sigma_R}{dE}$
- double differential cross section in both solid angle and energy $\frac{d^2\sigma_R}{d\Omega dE}$

They represent the probability for a given reaction to occur in the intervals $[\Omega;\ \Omega{+}d\Omega]$, $[E;\ E{+}dE]$ or both. Integrating on both intervals it is possible to obtain the cross section:

$$\sigma_R = \int_0^{\Omega} \int_0^{E_{max}} \frac{d^2\sigma_R}{d\Omega dE}\, d\Omega dE. \tag{1.10}$$

Summing over all possible reactions we obtain the *total cross section* of fragmentation:

$$\sigma_{tot} = \sum \sigma_R. \tag{1.11}$$

According to the exponential law, starting with an initial number of particles N_0 which traverse a medium with thickness x, the expected number of particles which had no interactions can be calculated as follows:

$$N(x) = N_0 e^{(-x/\lambda)} \tag{1.12}$$

where λ is the *mean free path* for a given total reaction cross section. Despite that theoretical knowledge of these fragmentation processes is poor, several reaction cross sections have been measured in these decades and parametrizations are available, too. Notably, the Bradt-Peters equation [9] is considered to be a good parametrization:

$$\sigma_R = \pi r_o^2 c_1(E) \left[A_p^{1/3} + A_t^{1/3} - c_2(E) \right]^2 \tag{1.13}$$

where A_p and A_t are mass number of projectile and target, respectively, r_0, c_1 and c_2 are parameters depending on the model.

1.3 Hadrontherapy

Hadrontherapy is a cancer treatment which uses a beam of charged hadrons to deliver a certain amount of dose to the tumor region of a patient. The first idea dates back to the 50's of the previous century from Robert Wilson [10] and only some years later the first clinical trial accomplished at the Lawrence Berkeley Laboratory, using the experimental cyclotron to produce a beam of protons for medical purposes [11]. From that time on, a lot of improvements were reached by researchers, as well as very promising results in clinical treatments. For these reasons, many hadrontherapy centers were built worldwide.

As of 2022, there are 114 facilities (with other 36 under constructions) [12], among which three are operating in Italy: CNAO (Centro Nazionale di Adroterapia Oncologica) [13] set in Pavia which provides beam of protons and ^{12}C ions taken by a synchrotron, Centro di Protonterapia in Trento [14] which exploits proton beams delivered by a cyclotron and CATANA (Centro di AdroTerapia ed Applicazioni Nucleari Avanzate) [15] in Catania, which uses protons accelerated by a superconducting cyclotron to treat ocular neoplasic diseases. Today only p and ^{12}C ions are used to treat solid tumours, but other particles such as neutrons, He and other light ions nuclei (like Li, O, up to Si ions) have been either used, or planned to be used, for future clinical treatments.

The main advantage of hadrontherapy relies upon the way energy is released in matter by hadrons, as described in the following paragraphs.

1.3.1 Bragg Peak

In radiobiology, the effects of radiation on the human body is given in terms of *dose*, which is the energy absorbed by the tissue per unit mass:

$$D = \frac{\mathrm{d}E}{\mathrm{d}m} \tag{1.14}$$

and it is measured in *Gray* (1 Gy = 1 J/kg). For charged particles, the energy absorbed by tissues is very close to the one released by the radiation and it is possible to find a relation between the dose and the mass stopping power:

$$D = \frac{\mathrm{d}E}{\mathrm{d}m} = \phi \frac{\mathrm{d}E}{\mathrm{d}x}\frac{1}{\rho} = \phi \frac{\mathrm{d}E}{\mathrm{d}\chi} \tag{1.15}$$

where ϕ is the fluence ($\frac{particles}{cm^2}$).

It is useful to associate the dose delivered in the medium to the crossed path (*depth-dose profile*), inferring from the Bethe-Bloch formula. As a charged particle enters the medium, it has a high velocity. While traveling, the particle starts losing energy (and thus delivering dose), but with a slow rise, since it is in the $\frac{\mathrm{d}E}{\mathrm{d}\chi} \propto ln(E)$ region. As the particle continues to lose velocity, it will reach the $\frac{\mathrm{d}E}{\mathrm{d}\chi} \propto \frac{1}{\beta^2}$ region. The dose delivered will then rise very quickly, until the particle slows down to a halt. As a consequence, the dose delivered is primarily localised at the depth where the particle stops, which is called *Bragg peak*. This behaviour can be seen in Fig. 1.4.

1.3.2 Spread Out Bragg Peak

The depth where the particle stops is another name for range, already defined in Sect. 1.1.3. By combining Eq. 1.2 with Eq. 1.5, it is possible to show that

$$R(E_k) \propto E_k^p \tag{1.16}$$

where E_k is the kinetic energy and p is a constant which depends on the incoming particle. For charged particles in human body, it is approximated as $R \propto E_0^{1.75}$.

This is a fundamental property to exploit in hadrontherapy because in order to reach a deeper region in human body, it is sufficient to increase the energy of the beam. This also solves another issue given by the dimension of tumors. In fact, the Bragg peak has a width of only a few millimeters, while the typical longitudinal depth of a tumor is of a few centimeters. However, by summing the contributions of multiple Bragg peaks at different energies, we obtain a Spread Out Bragg Peak (SOBP) [17] as seen in Fig. 1.5.

In order to obtain a SOBP, according to the provided accelerator, it is possible to apply a degrader on a fixed energy beam, which is spread on energy and no more monochromatic (with cyclotrons), or just accelerating particles with different energies, obtaining in this way a pulse flux (with synchrotrons) [19].

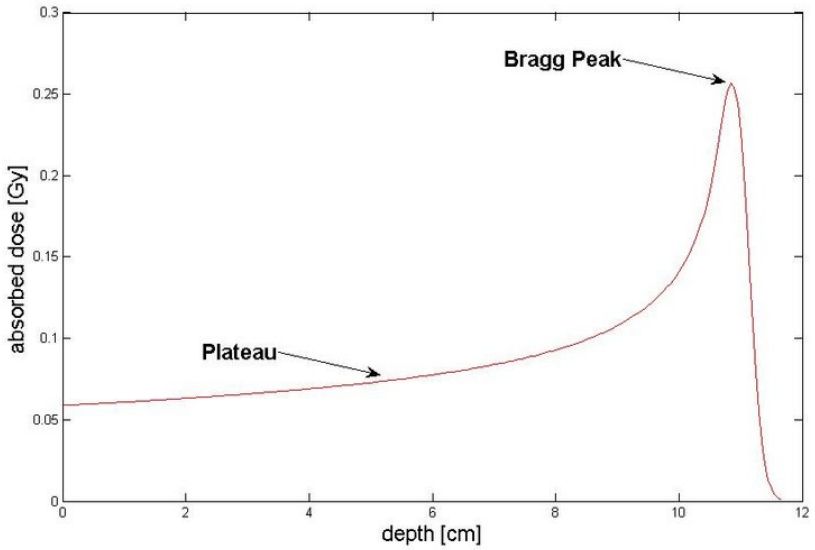

Figure 1.4: Absorbed dose of a monoenergetic proton beam as a function of depth. The Bragg peak is localised just before the particle stops [16].

1.3.3 Straggling

Despite being one of the crucial advantages of hadrontherapy, there is one problem with the Bragg peak: even a slight variation of the range risks overshooting the tumor and irradiating healthy tissues [20]. As mentioned in Sect. 1.1.3, the range straggling is directly related to energy-loss statistical fluctuations. The effect of the straggling on the shape of the Bragg Peak can be seen in Fig. 1.6.

It is also worth comparing hadrontherapy with the most conventional and well know radiotherapy. In conventional radiotherapy, a beam of gamma rays irradiates the tumor region. However, since photons are neutral particles, the depth-dose profile does not present a Bragg peak. Instead, it features a "wide" peak near the surface of the material and then it presents an exponential attenuation with a long tail. A comparison with respect to hadrontherapy is presented in Fig. 1.7.

Another aspect that can be inferred from Fig. 1.7 is the difference between protons and carbon ions. In fact, it is possible to see that carbon has a higher peak but a longer tail after the particle stops. This is a consequence of nuclear fragmentation, as illustrated in Sect. 1.2. Carbon can undergo nuclear fragmentation while crossing biological matter. This generates lighter projectile fragments that travel beyond the Bragg peak, causing the aforementioned tail. Protons instead only generate heavier target fragments that have a very short range. This explains the absence of the tail. In summary, there is a trade-off with using heavier ions: a sharper Bragg peak, but a longer tail.

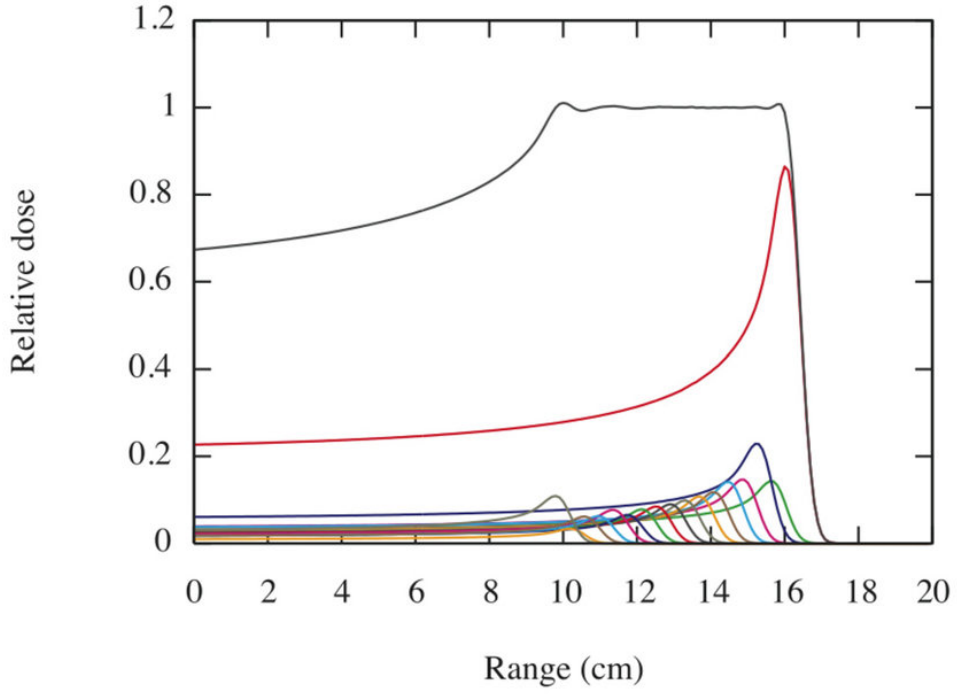

Figure 1.5: SOBP (in gray) obtained by superimposing Bragg peaks of different energies (in other colors) [18].

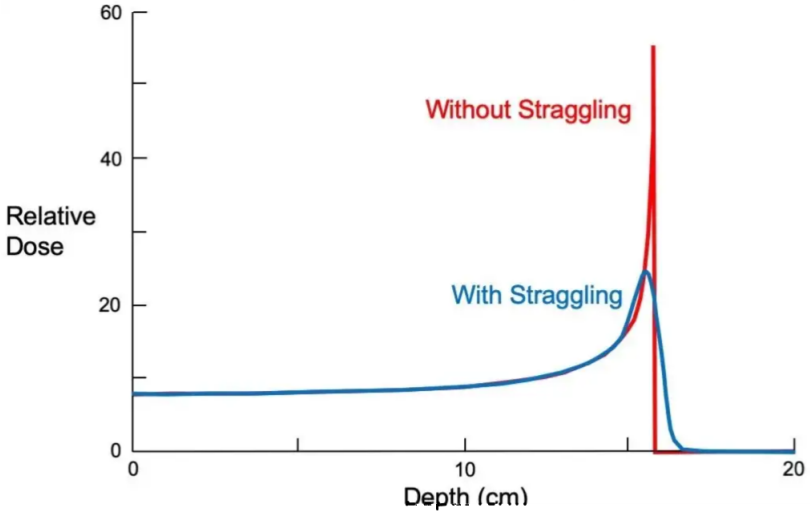

Figure 1.6: Relative dose as a function of depth. The Bragg peak with straggling (blue) is lower and has a longer tail than the one without straggling (in red).

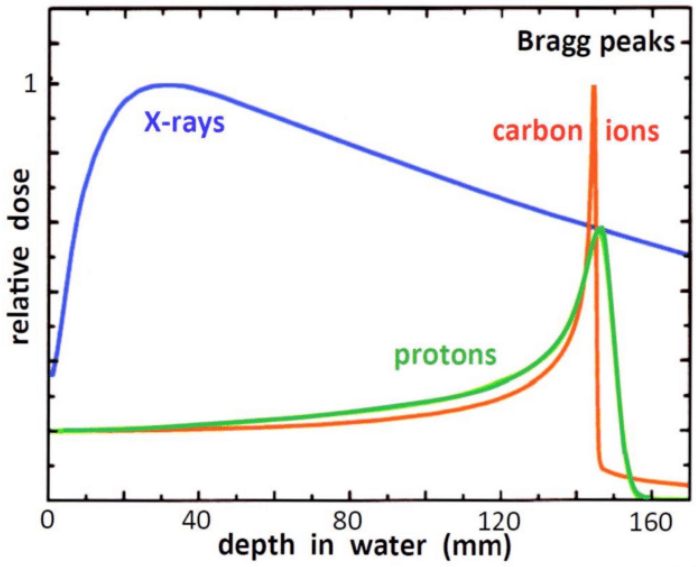

Figure 1.7: Depth-dose profile for photons, protons and carbon ions [21].

A release of dose after the Bragg peak due to projectile fragments is damaging for the healthy tissues beyond the tumor. Nevertheless, target fragments absorption by biological matter through all the path cannot be neglected in terms of effects [22]: since these collateral effects are present, it is fundamental to know the processes of nuclear fragmentation as best as possible, in order to limit the risk factor of the treatment.

1.4 Radiobiology

The main objective of cancer therapy with radiations is to kill tumor cells, or at least to prevent their duplication. This can be achieved with two different processes: the *direct* way and the *indirect* way.

In the direct way, the incident radiation hits the DNA molecules, ionizing them and breaking their chemical bonds. This process accounts for approximately 1/3 of all biological effects caused by ion irradiation. DNA damages can be mainly of two types: *Single Strand Breaks* (SSB) and *Double Strand Breaks* (DSB). Both can be repaired by DNA polymerases but DSB are much more difficult to repair, especially if they occur in clusters.

In the indirect way, the radiation hits the water molecules present in the cell, producing free radicals. This accounts for the remaining 2/3 of the biological effects [23]. In particular, the energy released during the interaction may free an electron, which can be captured by another water molecule:

$$H_2O \rightarrow H_2O^+ + e^-$$

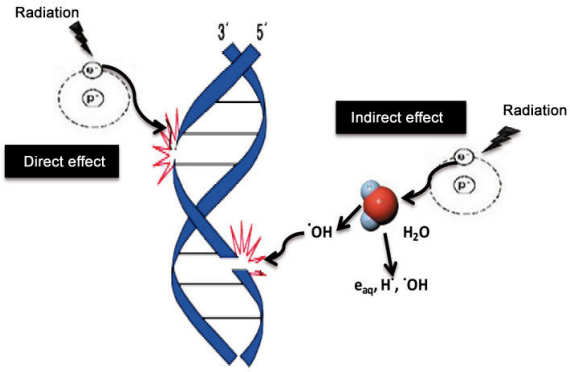

Figure 1.8: Direct and indirect ways for DNA damage.

$$H_2O + e^- \rightarrow H_2O^-$$

Now that H_2O^+ and H_2O^- are present, two reactions can occur:

$$H_2O^- \rightarrow H^\bullet + OH^-$$

$$H_2O^+ \rightarrow H^+ + OH^\bullet$$

where $H^\bullet$ and $OH^\bullet$ indicate free radicals, i.e. an atom or a molecule that has an unpaired valence electron. These molecules may recombine, forming two different products:

$$H^\bullet + OH^\bullet \rightarrow H_2O$$

$$H^+ + OH^- \rightarrow H_2O$$

which is harmless water, and

$$OH^\bullet + OH^\bullet \rightarrow H_2O_2$$

which is hydrogen peroxide, a highly toxic chemical for a cell. The combination of free radicals and H_2O_2 can damage the DNA strands, making SSB or even DSB. The effects of radiation on DNA can be seen in Fig. 1.8.

1.4.1 Linear Energy Transfer

The most important physical quantity in radiobiology is the dose deposited in tissue, as already defined in the previous section (Eq. 1.14). Another crucial quantity is the *Linear Energy Transfer* (LET) [24], a measure of the energy deposited by a particle traveling

through matter. It is related to the stopping power already defined in Sect. 1.1 and it is defined as the energy deposited per unit of length:

$$\mathrm{LET} = \frac{\mathrm{d}E}{\mathrm{d}l} \tag{1.17}$$

and it is measured in keV/μm. This definition, though, only considers the secondary electrons which deposit energy locally excluding those which have a longer path. While stopping power can be seen as a medium property which describes the energy absorbed by matter, LET describes the energy loss of the particle. If all the secondary electron energies are considered, LET equals stopping power.

Even though LET is not a good parameter to describe the full spectrum of biological radiation effects, it is still a widely used quantity to categorize radiation damage.

1.4.2 Linear-quadratic model

In order to quantitatively describe radiobiological effects, the Linear Quadratic (LQ) model was developed [25]. This model takes into account the fact that cell death follows random probability statistics (Poisson, in particular) because of the stochastic nature of radiation-induced ionization. It also takes in consideration the aforementioned difference between SSB and DSB: the former does not cause a lethal damage while the latter could. Considering these two factors, the radiation effect on a cell population can be expressed as the *survival probability*

$$S(D) = \exp(-\alpha D - \beta D^2) \tag{1.18}$$

where α and β are two constants and D is the dose. In particular, α shows the intrinsic cell radiosensitivity and depends on the proportion of cells that will die, while β reflects cell repair mechanisms and depends on the proportion of cells that will not die due to DNA polymerase. While α-value is more important for high-LET radiations, β-value is more important for low-LET ones, as can be seen in Fig. 1.9.

The ratio α/β is the value assumed by the absorbed dose for which the linear and quadratic components of cell death are equal. This quantity assumes different values according to the type of tissue considered: it is $0.5-6$ Gy for tissues with low reproduction activity, while it is $6-20$ Gy for tissues with high reproduction activity. Experimental data agree with LQ model over a wide range of dose and tissues. However, it does not take into account treatment time and dose rate.

1.4.3 Relative Biological Effectiveness

The *Relative Biological Effectiveness* (RBE) indicates the ratio between the dose of reference radiation D_{ref} (usually 250 keV X-rays) and the dose of the radiation under

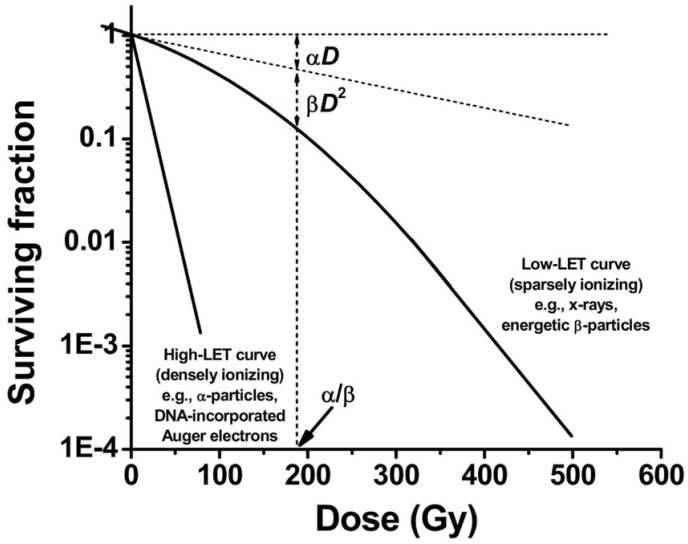

Figure 1.9: Survival curves for high-LET and low-LET radiation [26].

test D_{test} in order to obtain an identical biological effect:

$$\text{RBE} = \frac{D_{ref}}{D_{test}} \tag{1.19}$$

RBE can be studied as a function of LET, like seen in Fig. 1.10. A linear dependence can be observed for lower LET, then a fast increase up until a peak at around 100 keV/μm. For higher LET, it begins to decrease, because the dose is so high that most of it is superfluous in causing cell death. This is sometimes referred to as *overkill effect*.

1.4.4 Oxygen Enhancement Ratio

The environment in which a tumor cell proliferates is very important in deciding the treatment. The absence or presence of oxygen, for example, plays a determinant role, because biological effects on tissues will be different.

This oxygen effect is quantified by the *Oxygen Enhancement Ratio* (OER):

$$\text{OER} = \frac{D_{\text{hypoxic}}}{D_{\text{aerobic}}} \tag{1.20}$$

where D_{hypoxic} and D_{aerobic} are the doses in hypoxic and normal conditions, respectively, resulting in the same biological effect. We expect OER to be greater than 1. This is because a high concentration of O_2 in the water inside the cell will amplify the action of free radicals and produce more hydrogen peroxide, resulting in more cell damage. OER is effectively always higher than 1, but its value depends on LET, as shown in

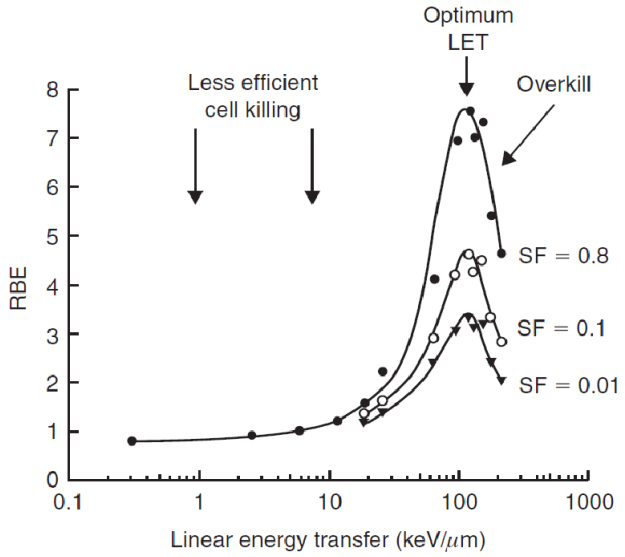

Figure 1.10: RBE as a function of LET for different survival fractions (SF) [27].

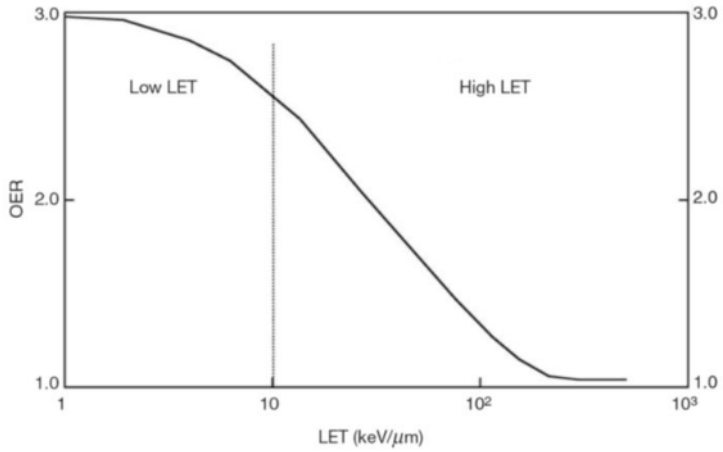

Figure 1.11: Oxygen Enhancement Ratio as a function of LET.

Fig. 1.11. The value of OER is 3 for low-LET radiation, but it decreases to near 1 for high-LET beams [28]. This is due to a saturation effect: at high-LET regimes, the hydrogen peroxide production is already very high, so the presence of oxygen does not increase significantly its production.

1.5 Inverse kinematics

A useful approach in fragmentation experiments is inverse kinematics, which consists in a role reversal between projectile particle and target particle. Operating in a reference frame in which the fragments are emitted from the target (which has become the projectile), they receive a Lorentz boost in the forward direction.

Let's consider **A**, a generic four-vector in the laboratory frame S:

$$\mathbf{A} = (a_t, \vec{\mathbf{a}})$$

where a_t is the temporal component and $\vec{\mathbf{a}}$ is the spatial vector. The Lorentz transformation of **A** from S to **A'** of the boosted S' reference frame is given by

$$\mathbf{A'} = \Lambda \mathbf{A}$$

where Λ is a 4×4 matrix. Considering the particular case where the motion is along the z axis, the transformation can be expressed as:

$$\begin{pmatrix} a'_t \\ a'_x \\ a'_y \\ a'_z \end{pmatrix} = \begin{pmatrix} \gamma & 0 & 0 & -\beta\gamma \\ 0 & 1 & 0 & 0 \\ 0 & 0 & 1 & 0 \\ -\beta\gamma & 0 & 0 & \gamma \end{pmatrix} \begin{pmatrix} a_t \\ a_x \\ a_y \\ a_z \end{pmatrix} = \begin{pmatrix} \gamma a_t - \beta\gamma a_z \\ a_x \\ a_y \\ -\beta\gamma a_t + \gamma a_z \end{pmatrix} \tag{1.21}$$

where $\beta = v/c$, v is the velocity of the system S' with respect to S and $\gamma = 1/\sqrt{1-\beta^2}$.

The matrix Λ of the transformation has the property that:

$$\Lambda^{-1}(\beta) = \Lambda(-\beta) \tag{1.22}$$

therefore, the inverse transformation is:

$$\begin{pmatrix} a_t \\ a_x \\ a_y \\ a_z \end{pmatrix} = \begin{pmatrix} \gamma & 0 & 0 & +\beta\gamma \\ 0 & 1 & 0 & 0 \\ 0 & 0 & 1 & 0 \\ +\beta\gamma & 0 & 0 & \gamma \end{pmatrix} \begin{pmatrix} a'_t \\ a'_x \\ a'_y \\ a'_z \end{pmatrix} = \begin{pmatrix} \gamma a'_t + \beta\gamma a'_z \\ a'_x \\ a'_y \\ +\beta\gamma a'_t + \gamma a'_z \end{pmatrix} \tag{1.23}$$

Replacing the generic four-vector **A** with the space-time one $\mathbf{S} = (ct, x, y, z)$ or the momentum-energy one $P = (E/c, p_x, p_y, p_z)$, it is possible to obtain the kinematic information in the needed reference frame.

This approach is particularly useful when the momentum of the projectile particle is not sufficient to produce target fragments with enough energy to allow their detection. This is the case of processes where proton beams at therapeutic energy are involved: a carbon or oxygen target would produce very short range (order of tens of microns) and very low energy (few MeV) fragments, which would not even be able to leave the target itself (few mm thick).

The inverse kinematic approach can be pursued, studying the fragmentation of different ions beams (C, O, Ca, etc.) onto a target made of an hydrogen enriched compound, such as polyethylene (C_2H_4). The cross sections σ onto H can be extracted by subtraction [29] from the data obtained using a C_2H_4 target in combination with a pure C one:

$$\sigma(H) = \frac{1}{4}\Big[\sigma(C_2H_4) - 2\sigma(C)\Big] \tag{1.24}$$

The same method can be adopted to study the cross sections on oxygen, using a polymethyl methacrylate (PMMA) target, since it is composed of carbon, hydrogen and oxygen. However, the disadvantage of this strategy is that the resulting cross section uncertainties are the quadratic sum of the uncertainties of the two single targets, therefore very precise measurements are needed.

It is important to improve the knowledge about nuclear fragmentation in particle therapy to reduce as much as possible the damage to healthy tissues in cancer treatments. With this aim, the FOOT (FragmentatiOn Of Target) experiment will provide several cross section measurements relevant for hadrontherapy. The details of this experiment will be presented in the next chapter.

Chapter 2

The FOOT experiment

The FOOT (FragmentatiOn Of Target) experiment has been designed to detect, track and identify charged fragments produced in ion collisions with different targets, with the aim of measuring both projectile and target fragmentation cross sections. These results are of primary importance in order to improve knowledge about nuclear interactions taking place in the patient and in order to account for fragmentation effects during the treatment planning. In fact, not all fragmentation processes have been investigated by experimental measurements, especially in the energy range useful for therapeutic application (50 - 250 MeV for protons and 50 - 400 MeV/u for carbon ions).

The target fragmentation measurement is an exceptionally challenging task because of the very short range of the produced fragments that results in a very low probability of escaping the target. Their range is confined to tens of microns and even a very thin solid target would stop them or badly spoil their energy measurement. This experimental problem can be overcome by using an inverse kinematic approach, studying the fragmentation of different ion beams (like ^{12}C and ^{16}O) onto hydrogen enriched targets, such as polyethylene (C_2H_4). The proton-Nucleus cross sections can be extracted by subtraction from data taken on C_2H_4 and C targets. The choice of beams is given by the need to simulate a patient: since over 93% of human mass is made of oxygen, carbon and hydrogen, and since protons do not fragment, C and O beams are used.

The FOOT detector is capable of performing the target fragmentation measurement using the inverse kinematic approach, but it can as well perform the direct measurement of projectile fragmentation cross sections induced by C, He and O beams, on the same graphite and polyethylene targets. Using different target materials, like polymethyl methacrylate (PMMA, $C_5O_2H_8$), also the collisions with other nuclei of interest for biological effects, like oxygen, can be studied.

2.1 Design criteria

The FOOT apparatus has been built taking in consideration specific requests, both from a practical and a scientific perspective. Since it needs to be transported to different research and treatment centers, its dimensions are limited. Nevertheless, to obtain the expected results, it is necessary to reach the following levels of precision [30]:

- momentum resolution $\sigma(p)/p \sim 5\%$
- time of flight resolution $\sigma(T_{tof}) \sim 100$ ps
- kinetic energy resolution $\sigma(E_k)/E_k \sim 2\%$
- energy release resolution $\sigma(\Delta E)/\Delta E \sim 5\%$

These quantities are needed to accurately measure fragment charge and mass in both direct and inverse kinematics. The fragment mass identification (mass ID or isotopic ID) is performed redundantly combining the measurements of the particle momentum, kinetic energy and time of flight, as described by the following relations:

$$p = mc\beta\gamma$$
$$E_k = mc^2(\gamma - 1)$$
$$E_k = \sqrt{p^2c^2 + m^2c^4} - mc^2$$

where $\beta = v/c$ and $\gamma = 1/\sqrt{1-\beta^2}$ are derived from the fragment time of flight. The redundancy is employed to reduce systematic errors as much as possible, which is necessary to reach the aforementioned levels of precision despite the minimal dimensions of the apparatus.

The charge ID, instead, is derived from the Bethe-Bloch formula (Eq. 1.2) after the evaluation of the energy loss and the time of flight.

2.2 Detector setup

To measure the fragment production due to protons and heavy ions, it is necessary to use beams of carbon and oxygen ions with energies about 100-400 MeV/u. For this purpose, three facilities have been chosen to be the most suitable locations for the FOOT experiment, since they employ ion beams with energies and resolutions typical of hadrontherapy treatments: CNAO (Centro Nazionale di Adroterapia Oncologica, Pavia, Italy), a hadrontherapy center which employs p and C beams; HIT (Heidelberg Ion-Beam Therapy Center, Heidelberg, Germany), a treatment facility that uses p, He, C and O beams; and GSI (Gesellschaft für Schwerionenforschung, Darmstadt, Germany), a research center equipped with, among others, an O beam.

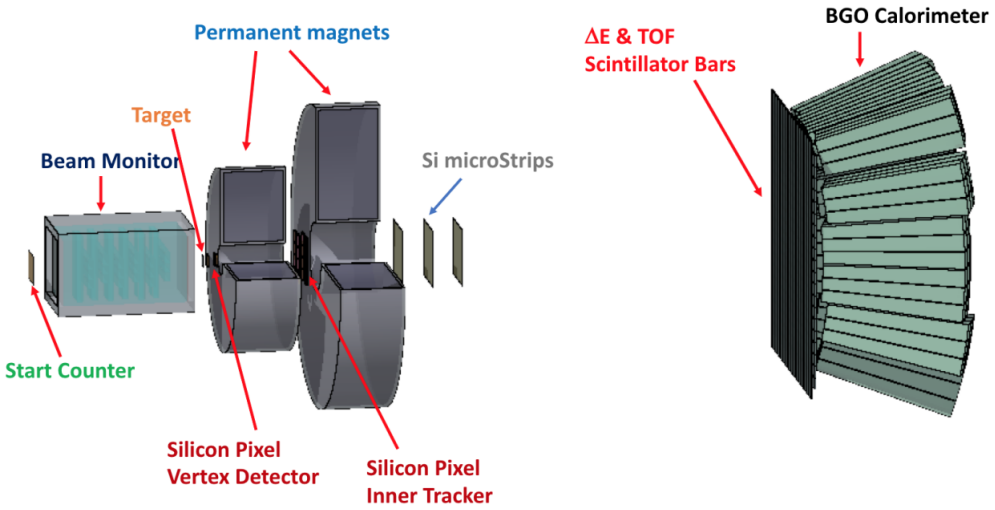

Figure 2.1: A schematic view of the FOOT electronical setup [30].

Considering the dimensions of the available experimental rooms, all the detectors have to be allocated in an approximately 2 meter length along the beam line. Thus the experimental setups have been designed in order to be easily movable ("table top setup") fitting the space limitations and covering the fragments angular spread. In particular, FOOT was designed in two alternative configurations: an electronic setup and an emulsion setup.

The electronic setup employs a magnetic spectrometer for track reconstruction and particle identification. This setup has been optimized for particles with a charge $Z \geq 3$ and has an angular acceptance of approximately 10° with respect to the beam axis. The emulsion setup uses an emulsion chamber spectrometer that is capable of identifying fragments with $Z \leq 2$ and has an angular acceptance of up to approximately 70°.

The focus of this thesis in on the electronic setup, so further details are provided here, while the emulsion apparatus is discussed in [31]. The electronic setup can be divided into three main regions: an upstream region, a tracking region and a downstream region, as shown in Fig. 2.1.

2.2.1 Upstream region

The upstream region is a pre-target region designed to monitor the primary beam. It is made up of two detectors: the Start Counter and the Beam Monitor.

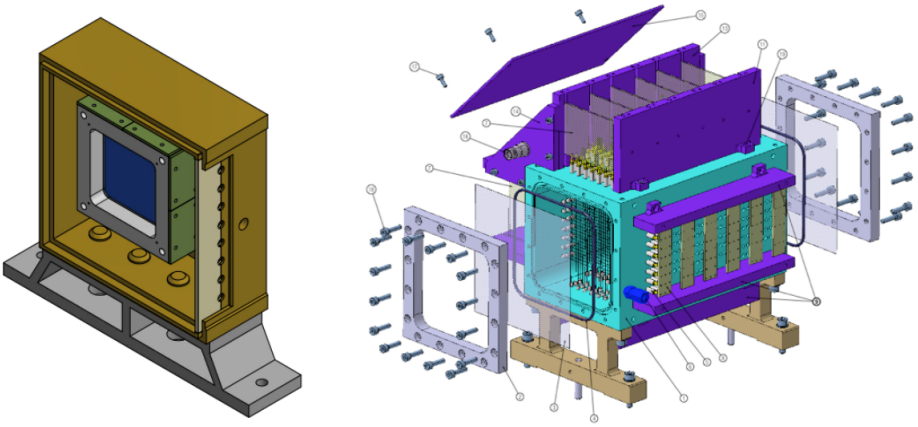

Figure 2.2: Schematic view of the Start Counter inside its frame (left) and technical drawing of the Beam Monitor (right) [30].

Start Counter

The Start Counter (SC) is made of a thin squared foil (5 cm side, 250 μm thickness) of EJ-228 plastic scintillator. The scintillator foil is held by means of an aluminum frame enclosed in a black 3D printed box to provide the light tightness needed for the detector operation (see Fig. 2.2 left). In the black box, two squared windows are placed in correspondence of the scintillator field of view and closed with thin (4μm) aluminized mylar. The light produced in the scintillator is collected laterally by 48 3×3 mm^2 SiPMs, 12 per side, bundled in 8 channels, each reading an array of 6 SiPMs. The readout and powering of the SiPMs is handled by the WaveDAQ system [32], capable of sampling signals at rates up to 5 GS/s in a dynamic range of 1V.

The SC provides the trigger signal to the whole experiment and the measurement of incoming ion flux to be used for the cross section measurement. It provides the reference time for all the other detectors and allows the time of flight (TOF) measurement in combination with the TOF wall. According to latest results, the SC time resolution is lower than 45 ps with 400 MeV/u carbon ions.

Beam Monitor

The Beam Monitor (BM) is a drift chamber consisting of twelve wire layers, with three drift 16 mm × 10 mm cells per layer (Fig. 2.2 right). Planes with wires oriented along the x and y axes are alternated allowing the beam profile reconstruction in both views. In each view, two consecutive layers are staggered by half a cell to solve left-right ambiguities in track reconstruction. The BM operates at ∼0.9 bar with a 80/20% gas mixture of Ar/CO_2, at a working point ranging between 1850 and 2200 V, depending on the primary beam. The BM efficiency is higher than 90% for a wide range of beams

and energies while a lower limit on the spatial resolution of 100 μm, in the central part of the BM cell, has been achieved [33].

The BM detector is placed between the SC and the target and it is used to measure the direction and impinging point of the beam ions on the target, a crucial information needed to address the pile-up ambiguity in the tracking devices downstream the target and to discard events in which the beam has fragmented in the SC producing one or more deviated tracks. In order to discard pile-up vertices, an high precision alignment is required between the BM and the devices downstream the target. The BM high spatial resolution is fundamental to measure the direction of the fragments with respect to the beam with an accuracy of few mrad, needed to measure the kinetic energy of the fragments in inverse kinematic with the required resolution.

2.2.2 Tracking region

The tracking region is composed of the target, a magnetic spectrometer, and a series of detectors: the Vertex Detector, the Inner Tracker and the Microstrip Silicon Detectors.

Magnets

The need to keep the setup movable together with the tight constraints to reach the required momentum resolution, guided the choice for a permanent magnet. In order to avoid a magnetic system in vacuum without spoiling the resolution, two magnets in Halbach configuration were chosen: this configuration allows to add a tracking station inside the magnetic field. The first magnet has a gap diameter of 5 cm while the second one of 10.6 cm. They can provide respectively a maximum intensity of 1.4 T and 0.9 T along the y axis in the internal cylindrical hole. Each magnet will be made of twelve single units of Samarium-Cobalt, which maintains its magnetic properties also in high radiation environments. Thanks to a detailed field map (Fig. 2.3), it will be possible to reach the intrinsic achievable accuracy of about 10 μm. Moreover, both magnets can be vertically lifted of about 40 cm, allowing to align the whole magnetic spectrometer in specific runs without the magnetic field and to access easily to the detectors.

Vertex Detector

The Vertex detector (VTX) is a stack of four MIMOSA28 (M28) silicon chips belonging to the family of the CMOS Monolithic Active Pixel Sensors (MAPS), which are commonly used for experiments in particle and heavy ion physics. The architecture of the MIMOSA28 integrates a fast binary read-out and a zero suppression logic to reduce the amount of data produced. Inside the read-out board there is the sensor, which is composed of a 928 $\times$ 960 matrix of pixels, 20.7 μm pitch, for a total sensitive area of 20.22 mm $\times$ 22.71 mm. Each sensor is 50 μm thick. The detector guarantees a geometrical

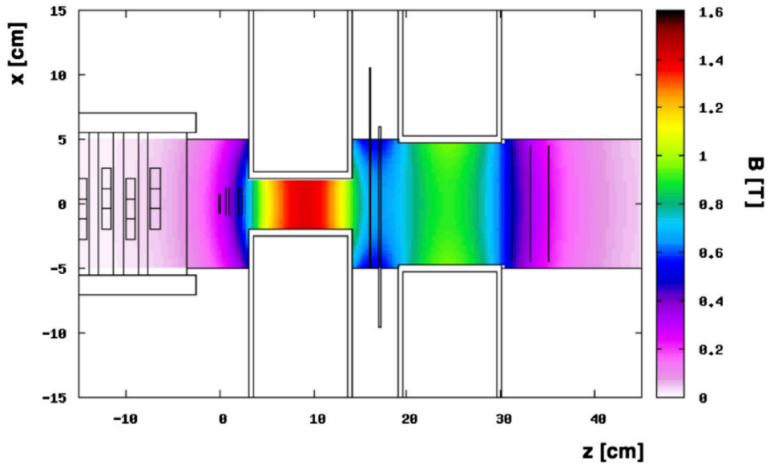

Figure 2.3: Computed magnetic field map of the two magnets in Halbach configuration [30].

acceptance of 40° and a spatial resolution of 5 μm [34], fulfilling the requirements of low material budget and high precision and efficiency. Figure 2.4 shows a geometrical scheme of the VTX and a picture of a M28 sensor.

Inner Tracker

The Inner Tracker (ITR) is the second detector of the tracking system located between the two magnets. Like the VTX, the ITR is made of M28 chips, but, accordingly to the emission angle, the fragment spatial distribution is broader at at this point, since the inner tracker is farther from the target (at a distance of about 16 cm) then the Vertex. For this reason, the area to be covered is larger and a different spatial configuration is needed. Each ladder is composed of two modules housing four M28 pixel sensors each. Four of these ladders will be placed as sketched in Fig. 2.5, implementing a double plane tracker that covers a total area of about 8 cm $\times$ 8 cm. In each module the four sensors are glued and bonded on a kapton Flexible Printed Cable (FPC), having two or three conductive planes and an overall thickness of about 100 μm. The two modules of the same ladder are glued on a 2 mm layer of silicon carbide low-density foam, which determines the distance between the modules. To minimize the horizontal dead area the distance between two consecutive sensors in the same module is about 30 μm.

Microstrip Silicon Detector

After the magnets, a third tracking station is present: this is essential both to measure the momentum of fragments and to match them with the hits in the ΔE-TOF detector and in the calorimeter. For such a tracking station a microstrip silicon detector (MSD),

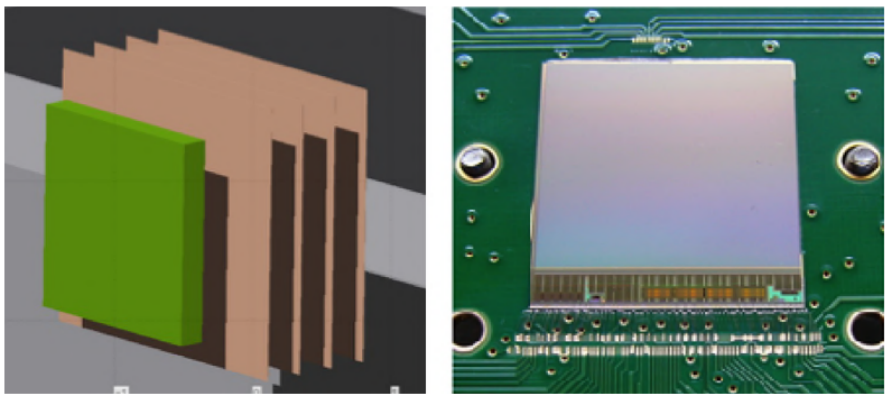

Figure 2.4: Target and vertex tracker geometrical scheme (left) and a M28 pixel sensor picture (right).

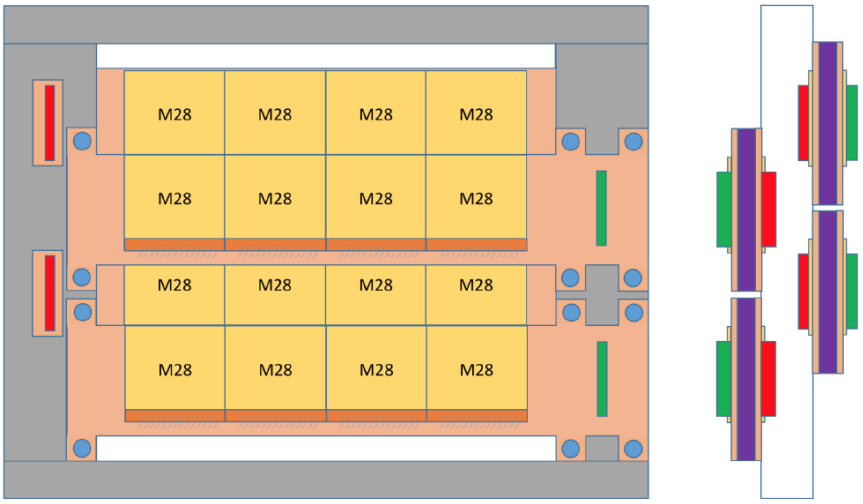

Figure 2.5: A schematic view of the Inner Tracker. On the right we see how the four modules are located in the global structure. Each module has two connectors, in red and green color, respectively on the front and back side of the ladder.

Figure 2.6: Picture of a MSD layer.

which can also provide a redundant measurement of $\frac{dE}{dx}$ thanks to its analog readout, was chosen (Fig. 2.6). The detector is composed of three x-y planes with an active area of 9.6 $\times$ 9.3 cm^2, separated by a 2 cm gap along the beam direction and positioned right after the second magnet. In order to reduce the amount of material and to provide the x-y coordinate readout, a setup with two perpendicular 150 μm thick Single-Sided Silicon Detector (SSSD) sensors has been adopted for each MSD x-y plane. A strip pitch size of 50 μm has been chosen in order to minimize the fragment pile-up in the same strip. For each SSSD, one every three strips is read for a total of 640 channels.

2.2.3 Downstream region

The downstream region is located at least 1 m away from the target and it is composed of two detectors: a plastic scintillator (also called ToF Wall) and a calorimeter.

ToF Wall

The ToF Wall detector (TW) is composed of two layers of 20 orthogonally oriented plastic scintillator bars (EJ200), each one 44 cm long, 2 cm large and 3 mm thick, coupled at both ends to four silicon photomultipliers (SiPMs) by means of an optical glue (Fig. 2.7). The scintillator is placed 1 m away from the target and it covers a square area of 40 cm $\times$ 40 cm, according to the fragments aperture at that distance. The TW has the purpose of both measuring fragments energy loss ΔE and crossing time, in order to stop the time of flight measurement. The detector granularity has been chosen according to the fragments expected separation at 1 m. The bars thickness, instead, is a compromise between the accuracy of ΔE measurements and the effort to reduce the

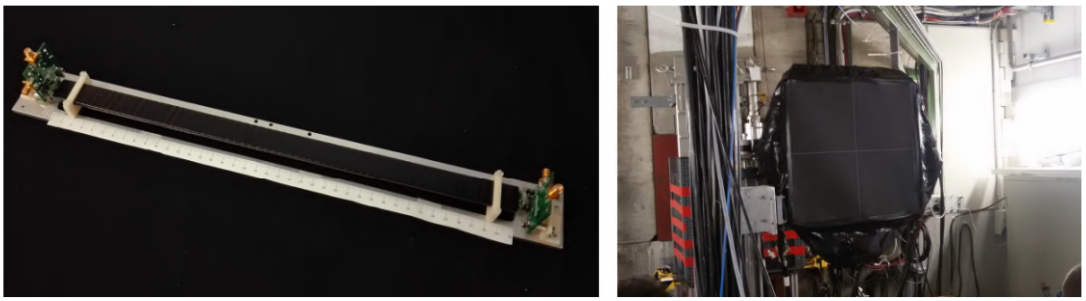

Figure 2.7: Picture of a EJ200 bar prototype (left) and the entire ToF Wall (right).

secondary fragmentation probability. In fact, a thicker bar would provide a higher light output and therefore an improved ΔE resolution but, due to the longer thickness to be traversed, it would also enhance the probability of re-fragmentation, thus spoiling the ΔE measurement. The simultaneous measurement of ΔE and TOF allows to identify the charge Z of the crossing ions [35]. The Z-identification plays a fundamental role in determining the fragment mass and is used, together with the x-y hit position, for the track reconstruction through the magnetic field.

Calorimeter

The calorimeter (CAL) is the most downstream detector. It will be composed of 320 crystals of bismuth germanate (BGO) arranged in a pointing geometry (Fig. 2.8). Each crystal is 24 cm long, with a front face area of about 2×2 cm^2 and an outer face area of 3×3 cm^2. Each BGO crystal is coupled to a 25 SiPMs matrix with an active surface of 2×2 cm^2. Each microcell has a 15 μm pitch, allowing to have a linear response in energy range up to about 10 GeV. At high energies, the interactions that happen inside the calorimeter are not only due to electromagnetic scattering, but also to hadronic scattering, so hadronic showers can be produced. As a consequence, together with the production of neutrons, particles can escape out of the calorimeter causing a systematic error that worsens the energy resolution. The depth of each crystal has been chosen in order to minimize the energy leakage. The CAL is designed to absorb completely the fragments in order to measure their kinetic energy, fundamental for the mass reconstruction.

2.2.4 Future developments

The FOOT apparatus is currently in a partial configuration because some subdetectors are still under development. In particular, the magnets are under construction and the 320 BGO crystals of the calorimeter will be finished in the near future. Several beam tests were performed at CNAO and GSI in order to optimize detectors configuration

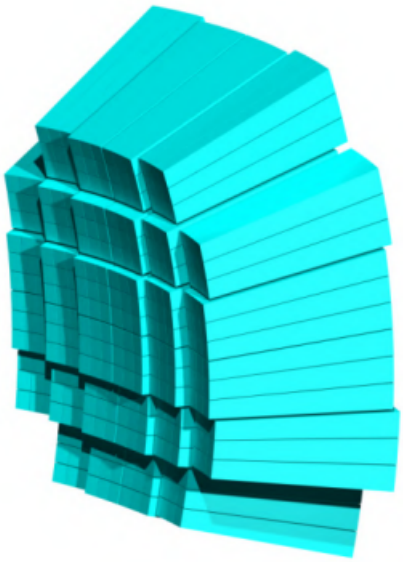

Figure 2.8: A schematic view of the calorimeter crystals setup.

and response, and other are already planned in the next months. Despite the partial configuration, three data takings for physics purposes have already been performed by the FOOT collaboration with electronic setup. The final campaign of data with the overall apparatus is foreseen for 2023 - 2024.

Chapter 3

Procedure

The purpose of this thesis is to study the effects of out-of-target fragmentation on the measurement of the cross section in the FOOT experiment. In particular, this work is focused on the data acquired at the GSI laboratory in Summer 2021. Details of both the analysis chain and my personal contribution will be described in the following pages.

3.1 GSI 2021

As mentioned in Chapter 2, the GSI facility in Darmstadt, Germany, is one of the research centers chosen for the FOOT experiment data taking. It is equipped with a heavy ion accelerator, which is used for nuclear structure and reaction experiments [36]. It is composed of a linear accelerator of 120 meters length, followed by a synchrotron with a circumference of 216 meters. It can accelerate a wide range of ions, from proton to Uranium, to velocities close to the speed of light.

In July 2021, some measurements were performed by the FOOT experiment with a partial setup, consisting of the following detectors: the Start Counter, the Beam Monitor, the Vertex, the Micro Strip Detector, the ToF Wall detector and 9 of the 320 BGO crystals of the calorimeter (Fig. 3.1). The target were made of both graphite (C) and Polyethylene (C_2H_4). A beam of ^{16}O at energies of 200 MeV/u and 400 MeV/u was used, for a total of more than 40 millions events in several configurations. The missing systems were still under construction, in time with the expected deadlines.

The main drawbacks of the FOOT setup at GSI were the absence of the magnets and the limited BGO configurations. No magnets means no momentum reconstruction, and the minimal BGO configuration only allows for kinetic energy measurement with a limited angular acceptance. Nevertheless, this data acquisition was fundamental not only for several detector studies and calibrations, but also for preliminary fragmentation cross section measurements.

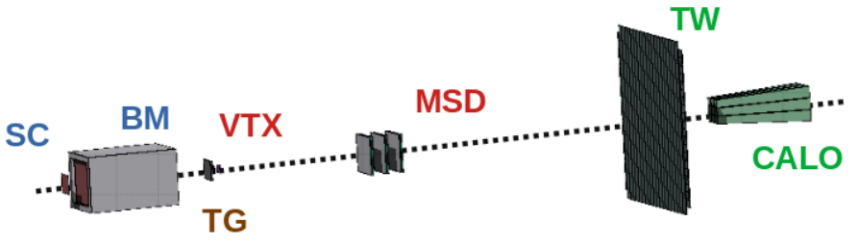

Figure 3.1: Schematic view of the partial FOOT electronic setup for the GSI 2021 campaign.

3.2 Software

SHOE (Software for Hadrontherapy Optimization Experiment) is a C++ object-oriented software, based on the ROOT framework [37], developed by the FOOT collaboration. The software is designed to take care of all the reconstruction steps for all the subsystems. Its final aim is the full reconstruction of both real and simulated events for cross section measurements. It is currently stored in a INFN git repository [38].

3.2.1 Simulation

The FOOT Monte Carlo simulation was generated using FLUKA simulator [39], which is partially integrated in SHOE. In both cases, the simulation follows a similar process:

- a detailed description of the experimental setup has to be provided and compared to the description given as input. This includes the full geometry and materials of the detectors and are necessary to correctly evaluate physical interactions.
- the Monte Carlo code generates beam particles and simulates energy loss, nuclear interactions and fragmentation. For each particle, whether primary or secondary, all kinematic quantities, like momentum, velocity, initial and final position, are generated.
- all the results are stored in ROOT format for following reconstruction and analysis.

3.2.2 Reconstruction

The event reconstruction involves the handling of the input and output data from the different detectors passing from the apparatus electronic signals to physical quantities, like positions and charges, in order to obtain the identification of the fragments produced.

The code is divided in three parts:

- **Libraries**

  Libraries of general interest, containing the main classes used by the reconstruction code to generate the detector geometry. The GENFIT external libraries [40] are also here. GENFIT is an experiment-independent track-fitting toolkit that combines fitting algorithms, track representations, and measurement geometries into a modular framework.

- **Level 0**

  Reconstruction code that is in charge of the interpretation of both Monte Carlo and acquired data, digitization, alignment and clustering of the events. In this part the track reconstruction with Kalman Filter is performed. The signals collected during the data acquisition runs and MC simulations are decoded, the detector dependent calibration constants are applied and the output of each detector is organized in "Hit", "Cluster" and "Track" objects:

  - **Hit**: Signal recorded by individual detector elements (such as a pixel, strip or wire) caused by a charged particle passing through them.
  - **Cluster**: Group of adjacent hits that are likely to have been caused by a single particle, analyzed together to obtain more precise measurements of the particle's properties.
  - **Track**: Reconstruction of the path taken by a charged particle through a detector, formed by combining information from multiple clusters along the particle's trajectory.

- **High Level**

  Reconstruction code deputed to the fragment identification and the cross sections measurement. The data obtained from the different sub-detector units are combined, achieving the final FOOT measurement: the different fragments are identified and their cross section estimated.

At the end of the event reconstruction another ROOT file is created. It contains histograms and trees according to the user's needs. Moreover, an event display is available to view each event in a user friendly visualization, and it is useful to perform geometry and tracking checks. A visual summary of the reconstruction code of SHOE can be seen in Fig. 3.2.

3.2.3 Charge identification

As already mentioned, the identification of a particle's charge in the GSI2021 FOOT setup is completely dependent on the ToF Wall. In fact, it can quantify the energy loss

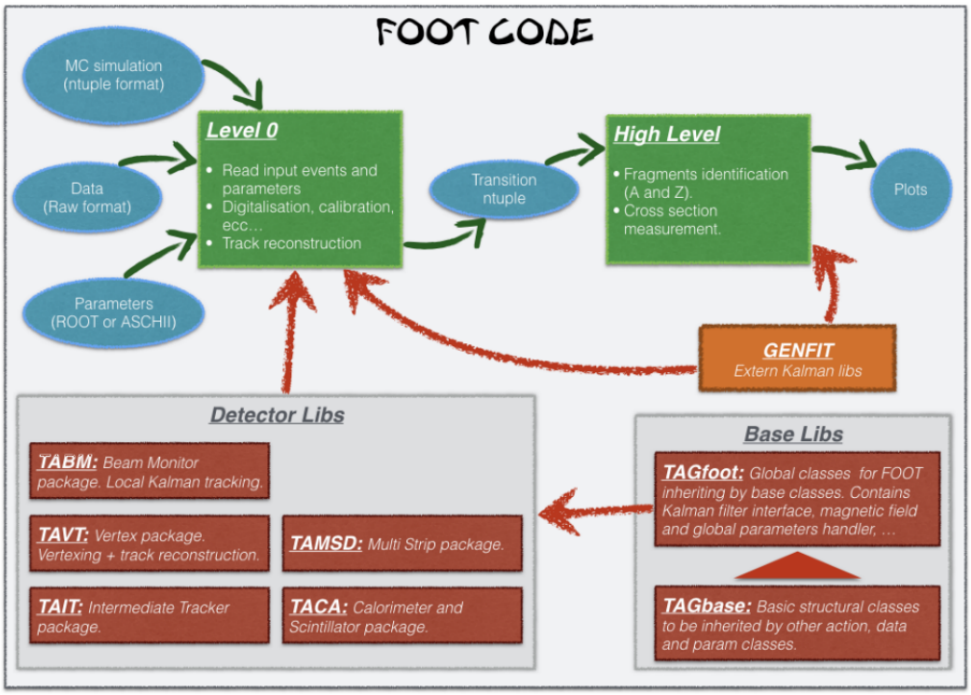

Figure 3.2: Diagram of the SHOE reconstruction code [41].

as well as the time of flight, by measuring the final time (the initial time is set by the Start Counter). Thus, the particle can be identified through its charge.

In SHOE, the charge identification algorithm uses the Bethe-Bloch formula (Eq. 1.2) through the $\Delta E - T_{tof}$ plot (Fig. 3.3). For every charge, a Bethe-Bloch curve is computed as a function of time of flight and energy lost. Since the Bethe-Bloch depends on $1/\beta^2$, the curves are proportional to T_{tof}^2. Then, the energy loss ΔE in the TW is calculated for each energy deposit left in the bars of the TW. The algorithm then proceeds to identify each fragment with the charge corresponding to the closest Bethe-Bloch curve.

The charge identification algorithm in SHOE can be applied to hits collected on each layer of the ToF Wall separately. Then, the algorithm can match those hit that should belong to the same particle, by looking at the position and the energy loss.

3.2.4 Tracking

Tracking refers to the process of calculating the trajectory of a particle through its interactions with different detectors. Many different physical properties can be calculated as a consequence, such as momentum, position and direction. The standard tracking methods estimate physical parameters through a minimization method like the Least Squares Method or the Maximum Likelihood Method, after all hits are considered. FOOT in-

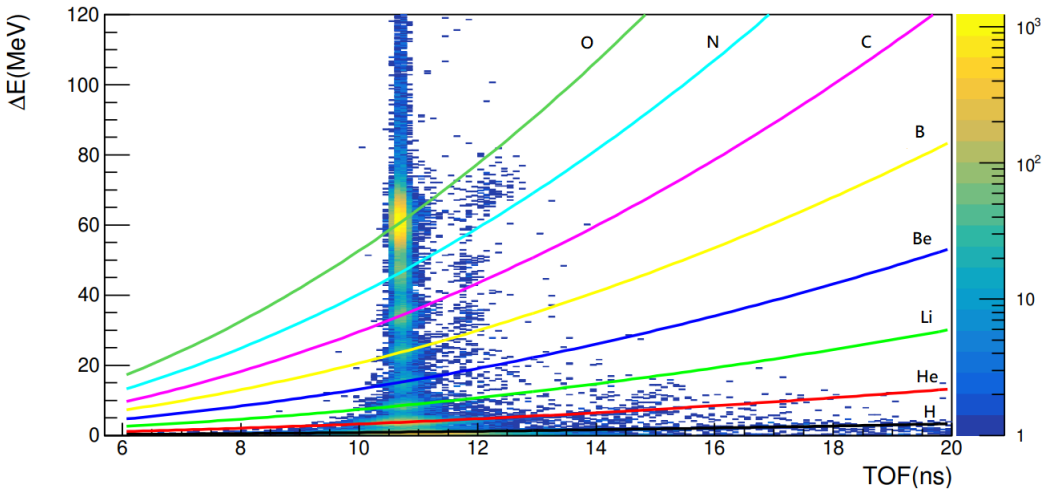

Figure 3.3: $\Delta E - T_{tof}$ plot for the GSI 2021 run. Each curve corresponds to a BB with different z [42].

stead uses a progressive method, in which the parameter estimation is improved after each successive hit. It is called Kalman Filter [43] and it is more flexible and powerful than standard tracking methods, as seen in Fig. 3.4.

The main steps in the Kalman Filter algorithm are prediction, filtering and smoothing:

- The track of the particle is considered a dynamic system, described by a state vector. The evolution of the state vector is given by a system of differential equations. The algorithm proceeds with propagating the state vector from point k to point $k+1$, corresponding to the following detector plane, obtaining a *predicted* hit.

- The algorithm then considers the measured hit on the detector plane and calculates a new point, a "compromise" between the measured and the predicted hit. This compromise is given by a χ^2 minimization method. This is the updated state vector that will be considered as a starting point for a following prediction. This process, called *filtering*, is illustrated in Fig. 3.5.

- After the prediction and filtering steps are done from $k = 0$ to $k = n$, the same steps are done backwards, from $k = n$ to $k = 0$. This process, called *smoothing*, is done to reduce the error, in particular on the first predicted points, where it is higher.

In SHOE, the Kalman Filter is implemented through the GENFIT software package [40], written in a C++ object-oriented design. Due to the absence of the magnets and the Inner Tracker, for the GSI 2021 run the trajectory is reconstructed using the hits in the MSD and TW.

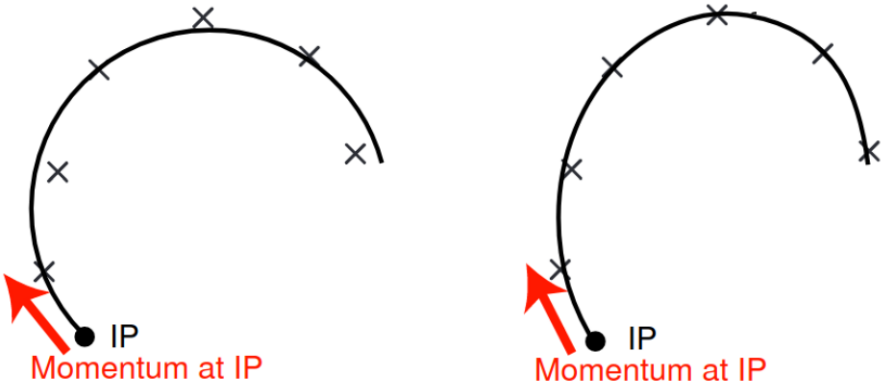

Figure 3.4: Least Square Method (left) for fitting of hits, compared to Kalman Filter (right). For the Kalman Filter, the parameters are defined for every hit [44].

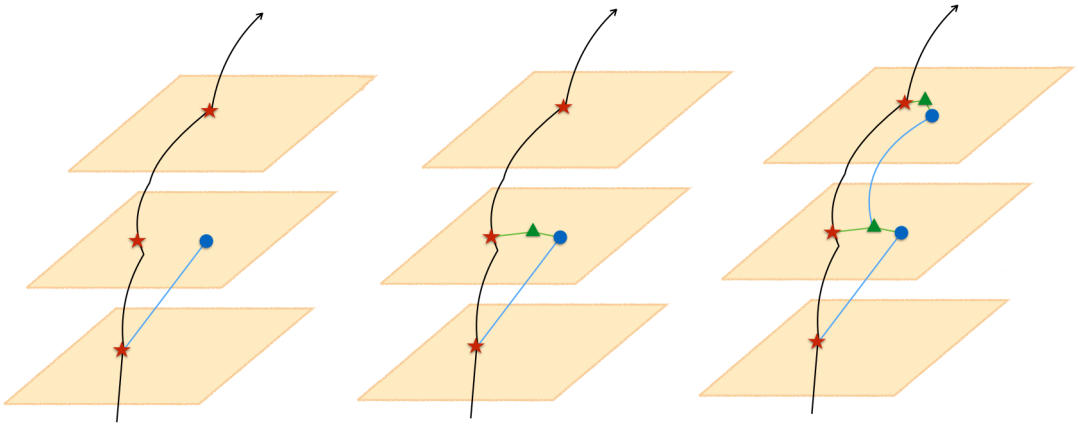

Figure 3.5: Schematic diagram of the prediction and filtering processes. Red stars are measured hits, blue dots are predicted hits and green triangles are filtered hits.

3.3 Out-of-target fragmentation

One important factor that needs to be considered in the FOOT experiment is that fragmentation does not only happen inside the target. Indeed, the beam particles could fragment in many other regions, such as:

- the detector planes, in particular those in the tracking region
- the magnets
- the air between each detector
- the air between each plane of a single detector

In addition, it is possible for target fragments to undergo secondary or tertiary fragmentation, complicating the topology of the event. This creates problems in fragment tracking and identification in many different steps of the process. First, out-of-target fragmentation may impact charge identification.

As already mentioned, the charge ID is given by the energy loss and the time of flight, both measured by the TW. If a particle fragments between the target and the TW, it may be incorrectly identified. This is because the fragmentation would generate particles with different velocities, making the estimate of β by the TW not correct.

Secondly, the Kalman Filter is designed to reconstruct the track of a fragment across multiple detectors, but at the moment is not equipped to deal with out-of-target fragmentation. In fact, the track reconstruction is expected to follow a single trajectory with no bifurcation given by fragmentations. An example of out-of-target fragmentation is shown in Fig. 3.6.

The problem with out-of-target fragmentation ultimately lies in being a background in event reconstruction, which, if not considered, may negatively impact the fragmentation cross section calculation. In this thesis, fragmentation in air and in detectors' materials are studied in order to find a simple selection to remove those events. The procedure adopted is described here.

3.4 Out-of-target identification strategy

For the purpose of this thesis, only simulated data of 400 MeV/n ^{16}O beam impinging on graphite are considered. The main steps of the analysis process are reported here.

- Firstly, a classification of the event types is devised. It takes in consideration where the beam particles fragment and gives an indication of the quality of the event for a future cross section analysis (Sect. 3.4.1).

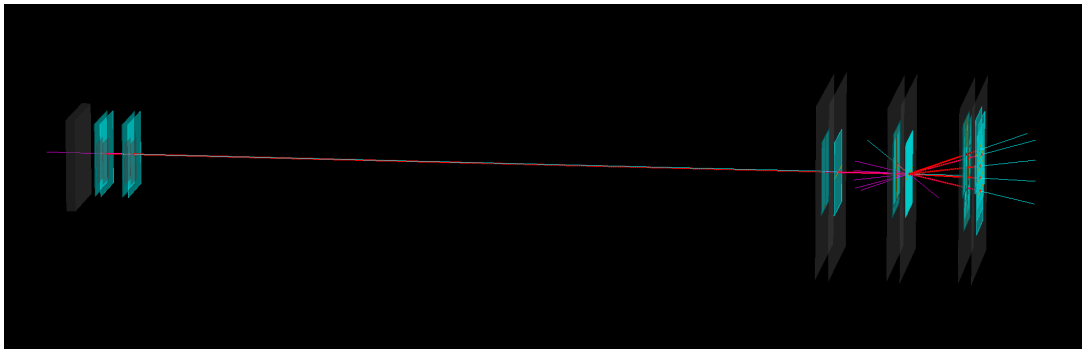

Figure 3.6: A fragmentation on the fourth layer of the MSD as seen in the SHOE event display. From left to right: the target, the 4 layers of the VTX and the 6 layers of the MSD. The beam comes from the left.

- Then, an algorithm is implemented in SHOE to apply the aforementioned classification in the track reconstruction step of the analysis (Sect. 3.4.2).
- The algorithm performance is then checked with Monte Carlo truth information. For this purpose, a similar algorithm is applied to MC generated particles (Sect. 3.4.3).
- The information on the event type is extracted from the algorithm and used in the global reconstruction analysis process. Finally, a comparison between reconstruction with or without selection on events is performed (Sect. 3.4.4).

3.4.1 Classification

The criterion of event classification was decided based on geometry and properties of the path taken by the fragment, depending on the region where the fragmentation happens. Events are then categorized in groups in order to study the track characteristics of each zone of fragmentation separately and use this information to optimize the event selection criteria. The goal is to select as many good events as possible (i.e., those resulting from target fragmentation) while rejecting as many out-of-target fragmentation events as possible. This optimized selection process can help to improve the overall quality of the data and increase the sensitivity of the FOOT experiment to nuclear in-target fragmentations.

The five event types of the classification are described here and summarized in Table 3.1.

- **Type 1**: These are considered good events, as they are the expected events that the FOOT experiment was designed to detect and study. These include events

where the beam particles do not undergo fragmentation and reach the ToF Wall, as well as events where all target fragments are tracked by every detector plane.

- **Type 2**: These are considered good events, similarly to Type 1 events, but not all fragments are tracked by every detector over the course of their flight to the TW. This is caused by either the fragments exiting the angular acceptance of the detectors or inefficiencies in detectors' clusterization algorithms.

- **Type 3**: These are bad events characterized by fragmentation on detectors' planes. This out-of-target fragmentation can be caused by beam particles or even by target fragments undergoing secondary fragmentation. The detectors considered in this study are the VTX and the MSD.

- **Type 4**: These are also considered bad out-of-target events where the beam particles or target fragments interact with air molecules, causing nuclear fragmentation. This can happen at any stage between the target and the TW.

- **Type 5**: These are bad events where no fragment or beam particle reaches the TW. For this events it is impossible to determine anything about the topology. Possible reasons for this occurrence are in-target and out-of-target fragmentations, angular acceptance, detector inefficiencies or a combination of all the above.

Event type	**Characteristics**	**Quality**
1	fragmentation in target, all particles tracked	good
2	fragmentation in target, some particles lost	good
3	fragmentation in detector plane	bad (out-of-target)
4	fragmentation in air	bad (out-of-target)
5	no point on the ToF Wall	bad

Table 3.1: Summary of event type classification.

3.4.2 Reconstruction algorithm

An algorithm for this event classification was introduced in the SHOE code and applied on the reconstructed information. The general logic followed by the algorithm is presented here.

First, a loop is performed on all detector sensors. For every detector, all hits corresponding to the passage of a particle are saved. Then, the total number of hits on each detector is calculated. At this point, the actual classification of events happens, as seen in Table 3.2. The classification algorithm mainly uses information given by hits on

detector planes. Type 1 events are events where the number of hits found on every layer of the three detectors used for the global tracking procedure remain the same, from the first VTX layer to the TW . If the number decreases from a layer to the following one, it means a fragment was probably lost, so it is tagged as a type 2 event. This means that the event is still good for further analysis, because an in-target fragmentation has happened and can be reconstructed. If the number increases, an out-of-target fragmentation has happened. If the number of hits increases between two layers belonging to different detectors, the fragmentation has probably happened in air, so it is labelled as type 4 event. On the other hand, if the number of hits increases between two successive layers of the same detector, the fragmentation probably happened on a plane of a detector, so it is labelled as a type 3 event. If no hits are detected on the ToF Wall, the event type is targeted as one of type 5.

Event type	**Condition**
1	n_{tot} remains constant
2	n_{tot} decreases between any two layers
3	n_{tot} increases between two planes of the same detector
4	n_{tot} increases between two different detectors
5	$n_{tot} = 0$ in the ToF Wall

Table 3.2: Summary of the reconstruction event classification algorithm. n_{tot} is the total number of hits for each detector plane.

3.4.3 Monte Carlo check

The previous algorithm is compared with information of the truth particle parameters given by the Monte Carlo simulation to check how good the selection manages to identify the out-of-target fragmentations. To this purpose, a similar algorithm was developed. Taking advantage of all the truth information about all simulated particles, it is possible to know where the fragmentation happened.

The most important parameters extracted from the MC simulation are given by `TAMCRegion` and `TAMCPart`. `TAMCRegion` contains information and methods about the regions in which the experiment is divided in. These regions are given by the geometry parametrization files, and they include air and every layer of each detector. In particular, `TAMCRegion` contains information on "crossings", which describe every instance of a particle going from a region to a different one. From each crossing, the main information that can be extracted are the regions where the crossing happens and the ID of the particle.

`TAMCPart`, instead, contains all information about a given particle for every event. These include the true charge, mass, initial and final position, and time of flight. One

particularly useful information for this study provided by `TAMCPart` is the region where the particle originates from: it can be either the primary beam, the target, each layer of every detector or air. The steps of the MC algorithm are illustrated here.

First, a loop on all particle crossings is done. For every crossing between air and sensor part of each detector, the algorithm saves the number and ID of particles that crossed. From the number of particles at each crossing, a first classification is done. If no particle crosses the ToF Wall, it is tagged as type 5. Furthermore, if the number of particle crossing decreases, a flag, noted as `lost_fragm`, is raised. Then, for each particle that crossed a region, the region of origin is determined. If it is air, the `air_fragm` flag is raised; if it is a detector, the `det_fragm` flag is raised instead. The event types 2, 3 and 4 are made to correspond to events with, respectively, `lost_fragm`, `det_fragm` or `air_fragm` flags raised.

An alternative classification is also introduced. New event types (6 through 9) are added to investigate all possible combinations of these flags. A summary with all the events is given in Table 3.3.

Event type	`lost_fragm`	`det_fragm`	`air_fragm`
1	`false`	`false`	`false`
2	`true`	`false`	`false`
3	`false`	`true`	`false`
4	`false`	`false`	`true`
6	`false`	`true`	`true`
7	`true`	`false`	`true`
8	`true`	`true`	`false`
9	`true`	`true`	`true`

Table 3.3: Summary of event type classification in MC. All combinations of the flags are considered.

3.4.4 Global reconstruction

After evaluating the accuracy of the algorithm, the event type is extracted using reconstructed variables and given as input in the global reconstruction analysis part of SHOE. Here, a selection on global tracks is performed based on the event type. The global reconstruction analysis, in fact, proceeds only if the event is of good, meaning of type 1 or 2. A comparison of the agreement of reconstructed and expected cross section is performed between all fragments and only the "good" ones. The difference in counting with or without selection is considered to calculate the cross section.

The comparison is performed on the elemental cross section, obtained from the angular differential cross section. The angular differential cross section is empirically defined

[45] as:

$$\frac{\mathrm{d}\sigma}{\mathrm{d}\theta} = \frac{Y(Z,\theta) - B}{N_{beam}\ N_{target}\ \Omega_\theta\ \epsilon(Z,\theta)} \tag{3.1}$$

where $Y(Z,\theta)$ and $\epsilon(Z,\theta)$ are respectively the number of fragments and the efficiency of a specific charge reconstructed in every event, B is the background present in each fragment production, Ω_θ is the phase-space, N_{beam} is the number of particles impinging on the target and N_{target} is the number of interaction centers in the target per unit surface. The total elemental cross section is then:

$$\sigma(Z) = \int_0^{\theta_{max}} \frac{\mathrm{d}\sigma}{\mathrm{d}\theta}\ d\theta = \frac{Y(Z) - B}{N_{beam}\ N_{target}\ \epsilon(Z)} \tag{3.2}$$

where θ_{max} is the maximum angular acceptance of the detector. N_{beam} is an information retrieved by the SC and BM and can be considered as the sum of all the selected events taking part in the analysis. Instead, the number of scattering centers N_{target} can be written as:

$$N_{target} = \frac{\rho \Delta x N_A}{A} \tag{3.3}$$

where ρ is the density, Δx is the target thickness, N_A the Avogadro number and A the mass number. In particular, for the graphite target $\rho = 1.83$ g/cm^3, $\Delta x = 0.5$ cm and $A = 12.0107$. The efficiencies ϵ are introduced dividing the number of fragments by the given factor for every bin of the distribution.

In the following chapter, all the results I obtained for this study are shown.

Chapter 4

Results

4.1 Classification analysis

A Monte Carlo dataset of 500 thousand events was generated by FLUKA to simulate the GSI 2021 campaign. The main results obtained following the procedure described in the previous chapter are shown here.

In Fig. 4.1a the event type distribution for reconstructed fragments is shown. It can be seen how the majority of events (over 97.5%) are reconstructed as type 1 or 2, meaning good events where the fragmentation happens inside the target and either all or some tracks are reconstructable. Only a small part (1.7%) are reconstructed as out-of-target fragmentation, in detectors (type 3) or air (type 4). Very low is also the number of reconstructed bad events of type 5 (0.8%), meaning events with no hit on the ToF Wall.

In Fig. 4.1b the same event type distribution is shown for MC fragments. Similarly to reconstructed fragments, 98.6% of events are of type 1 or 2. Type 3 or 4 events constitute 1.3% of events, while only 0.1% are of type 5. The noticeable difference between reconstructed and MC events of type 5 is probably due to inefficiencies in the clusterization algorithm of the ToF Wall.

In Fig. 4.2, the aforementioned distributions are plotted against each other in a matrix. This allows us to check whether the classification algorithm on reconstructed events correctly identifies the type for each event. What emerges is that the algorithm correctly identifies the vast majority of events of type 1 and 2. MC type 3 events are generally identified as reconstructed type 3, while most MC type 4 events are incorrectly identified. In fact there seems to be a mixing between MC type 4 and reconstructed type 2 events. Furthermore, all MC type 5 events are correctly classified, but not all reconstructed type 5 events are MC type 5. In fact, the majority of them are of MC type 1 and 2, so the selection rejects also some good events. To get rid of these mixings, improvements are needed on the clusterization algorithms of the MSD (for 2-4 mixing),

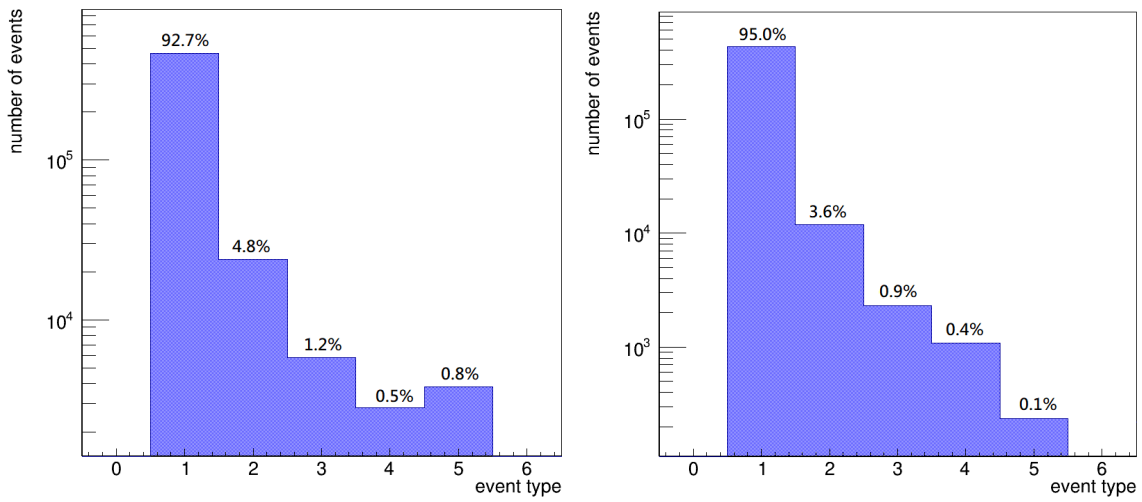

(a) Reconstructed events (b) MC events

Figure 4.1: Event type distribution for reconstructed and MC events. The percentage over total number of events is shown above each bar.

which is still being studied, and on charge reconstruction algorithm of the TW (for 1-5 mixing).

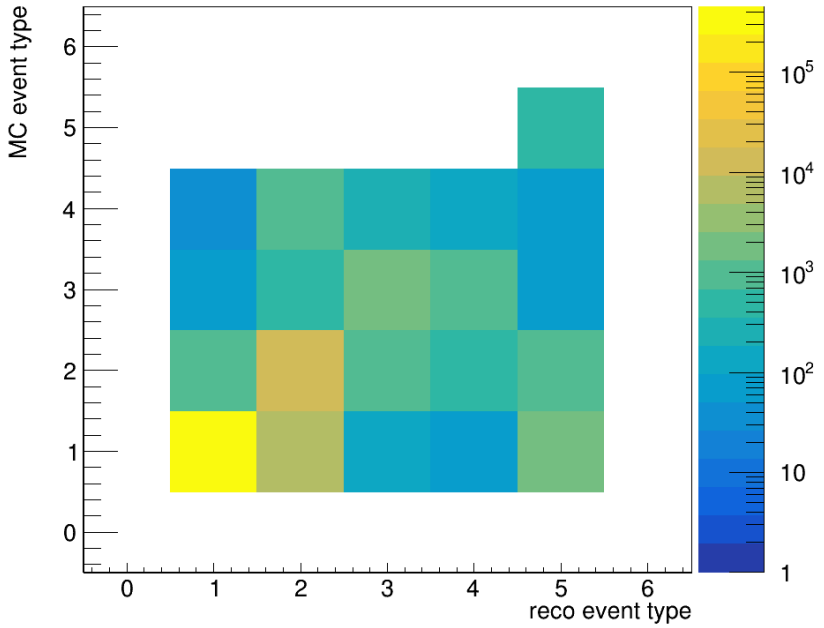

Figure 4.2: Event type matrix.

To further investigate the origin of this difference between the reconstruction based classification and the MC true one, it is useful to look at the behaviour of the additional categories in MC truth classification only, described in Sect. 3.4.3. Equivalent figures to the previous two are reported with the alternative classification in Figs. 4.3 and 4.4. From the former, it can be seen how combined fragmentations (type 6 and 9) are very rare, only constituting 0.1% of events. Type 7 and 8 are instead more common, comparable with type 4 events. Additionally, it emerges that nearly 37% of reconstructed type 3 events are MC type 8, meaning a combination of detector fragmentation and a fragment exiting the angular acceptance. In any case, this mixing is not a problem for a future analysis selection because it would not affect selection efficiencies and purities.

Another way to probe the accuracy of the classification algorithm on reconstructed events is to inspect the plane occupancies, meaning the number of clusters as a function of detectors' planes. In Fig. 4.5 all plane occupancies are shown for every reconstructed event type. On the x-axis the detector plane ID are present: 0 to 3 are the 4 planes of the VTX, 4 to 9 are the 6 planes of the MSD and 10 corresponds to the TW. Fig. 4.5a correctly shows how the number of clusters remains the same through every detector of the experiment, and that for 99.8% of events only one track is reconstructed. Fig. 4.5b shows an expected descending trend, but an increase is present in the first layer of the MSD and on the TW. This is probably related to the aforementioned mixing between type 2 and 4 and should be further investigated. Fig. 4.5c shows several increases inside the detectors, in particular between the first and the second layer of the MSD. Fig. 4.5d correctly shows an increase between the VTX and MSD and between the MSD and the TW. Fig. 4.5e, finally, shows all events with zero number of clusters on the TW.

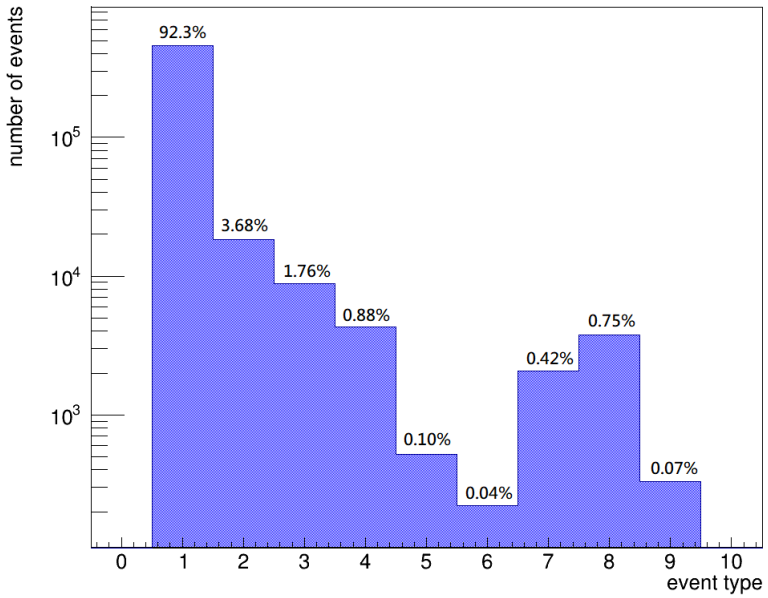

Figure 4.3: Event type distribution for MC events with the alternative classification. The percentage over total number of events is shown above each bar.

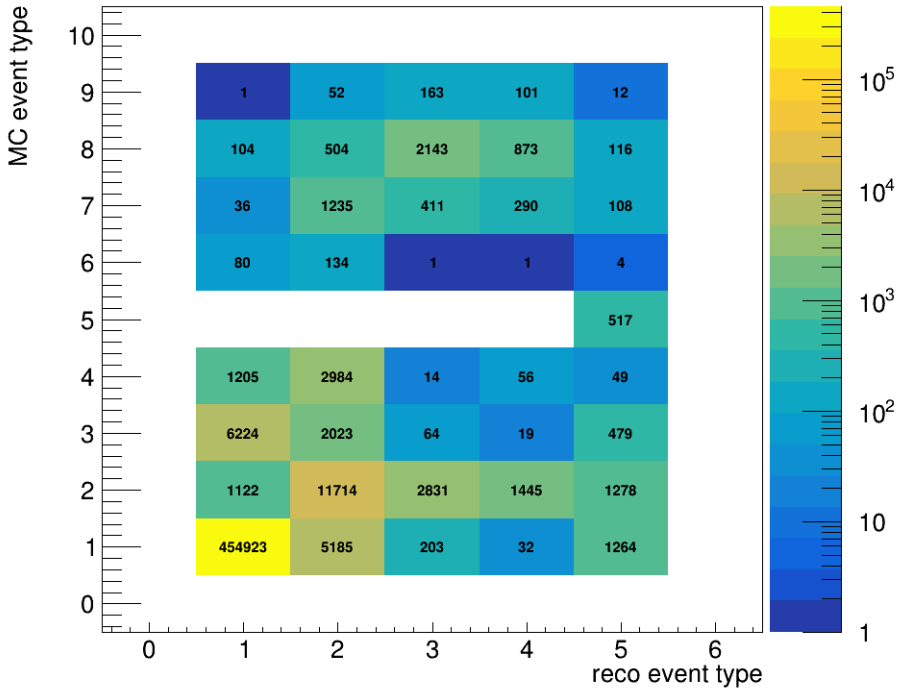

Figure 4.4: Event type matrix with the alternative classification.

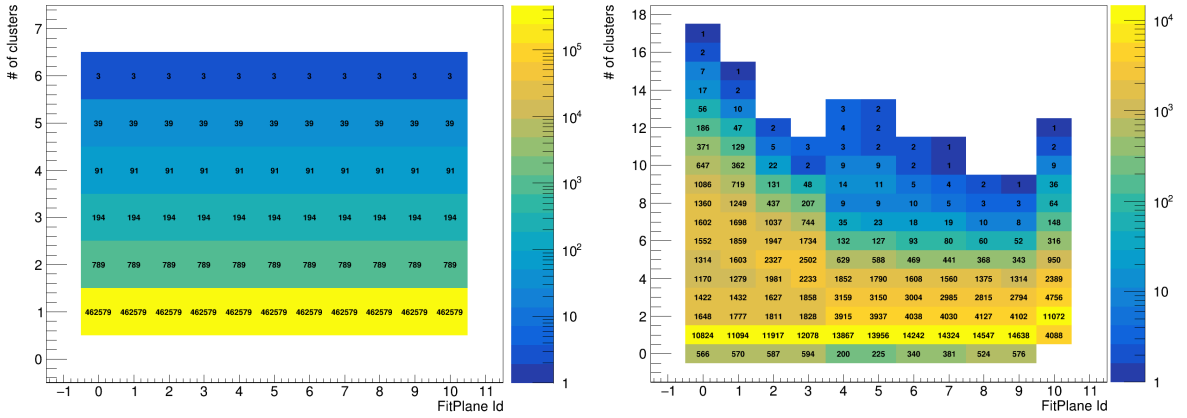

(a) Type 1

(b) Type 2

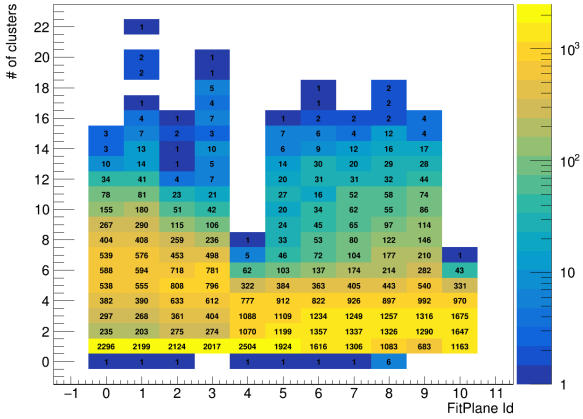

(c) Type 3

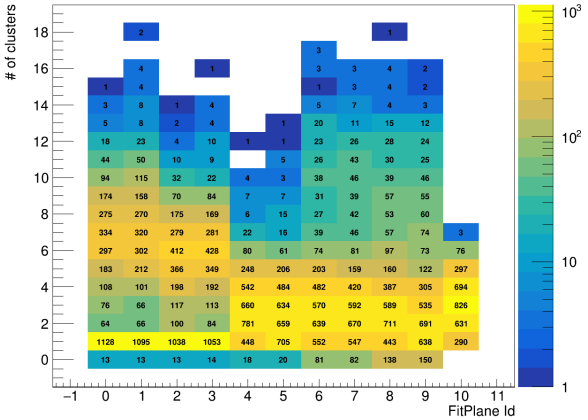

(d) Type 4

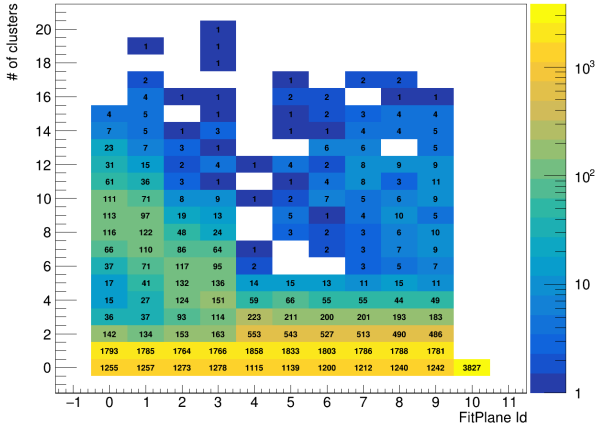

(e) Type 5

Figure 4.5: Plane occupancy for each reconstructed event type.

4.2 Selection analysis

After acknowledging the expected accuracy of a selection on only type 1 or 2, the global reconstruction analysis is performed. In Fig. 4.6 the number of reconstructed fragments for every charge are reported, with and without the selection on type. Fig. 4.6a shows all fragments, with a great reduction particularly on H and He. Fig. 4.6b shows only fragments that, using MC information, we know originate from out-of-target fragmentation. The reduction on out-of-target fragments is significant (over 50%) for all values of Z.

To correctly evaluate the effectiveness of the selection, the ratio of out-of-target fragments over all reconstructed fragments as a function of the charge is reported in Fig. 4.7. What emerges is that the selection greatly reduces this ratio, in particular for heavier fragments like C and N. This ratio is plotted also as a function of the angle of emission θ in Fig. 4.8. It can be noticed how the ratio is reduced by a larger margin at smaller angles, while it is already very low at higher angles. At higher angles, however the statistics is very low, in particular for heavier fragments.

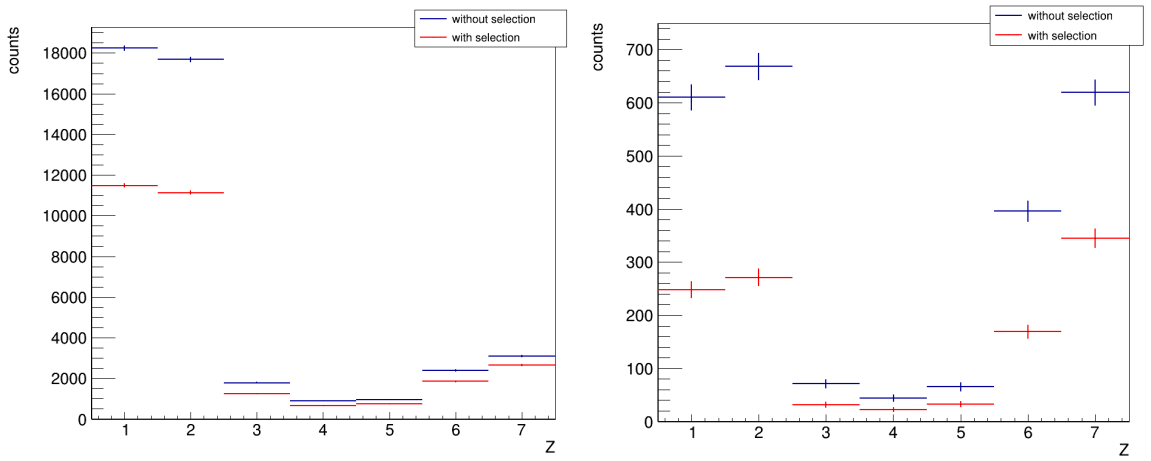

(a) All fragments. (b) Fragments originating outside the target.

Figure 4.6: Charge distribution of reconstructed tracks. In blue, the reconstruction is done without selection on event type. In red, only type 1 or 2 events are selected.

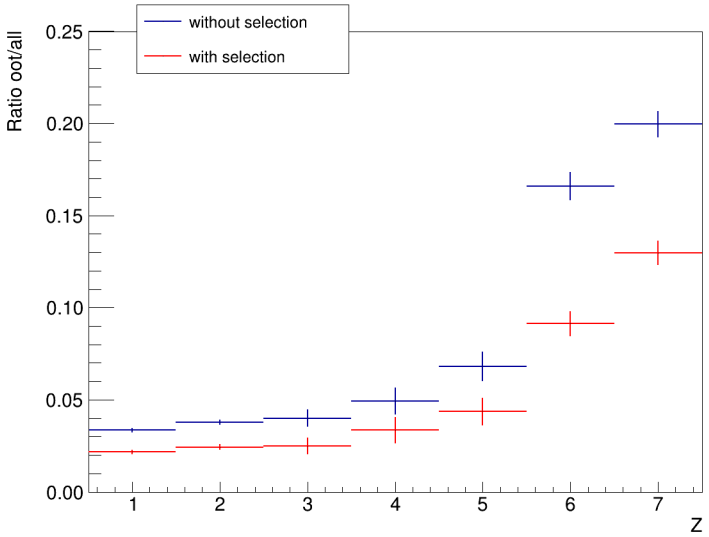

Figure 4.7: Ratio between counts of tracks originating outside the target over all tracks by charge. In blue, the reconstruction is done without selection on event type. In red, only type 1 or 2 events are selected.

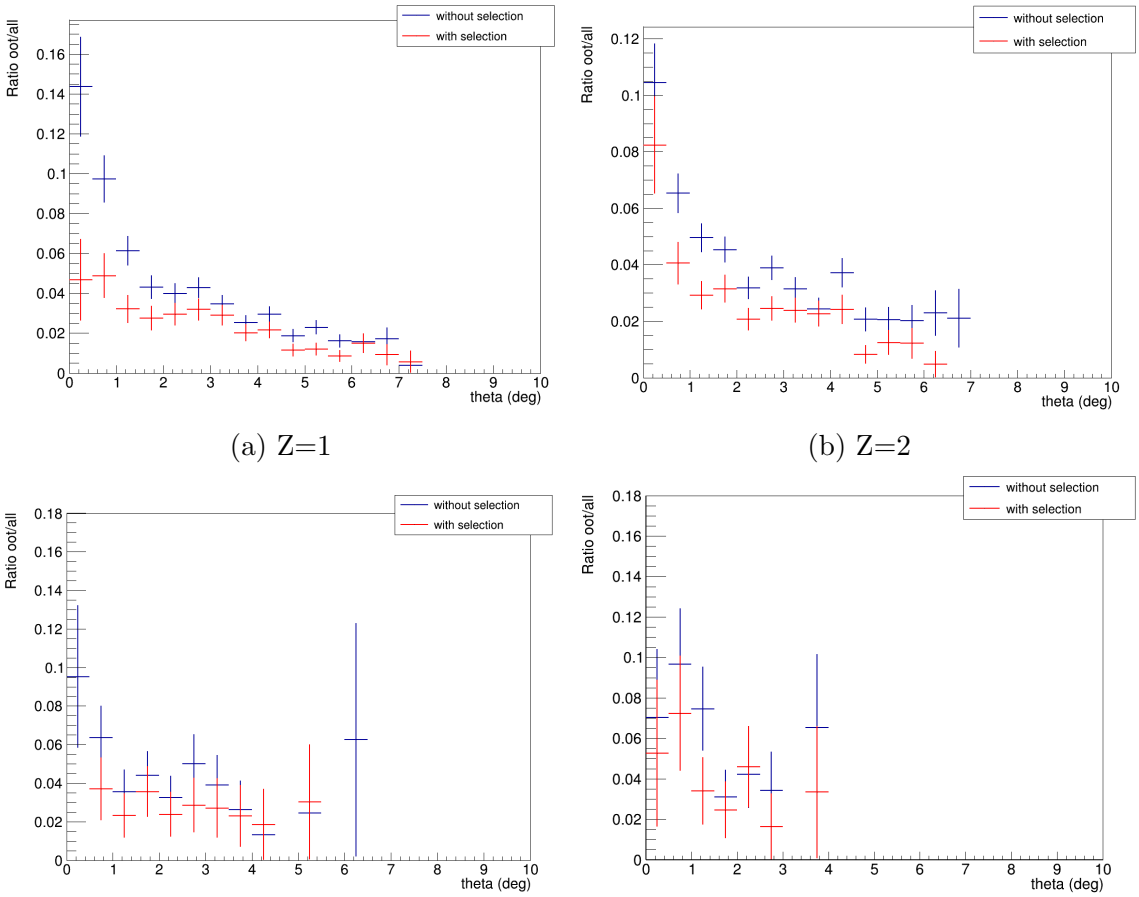

(a) Z=1

(b) Z=2

(c) Z=3

(d) Z=4

Figure 4.8: Ratio between counts of tracks originating outside the target over all tracks by angle for every charge. In blue, the reconstruction is done without selection on event type. In red, only type 1 or 2 events are selected.

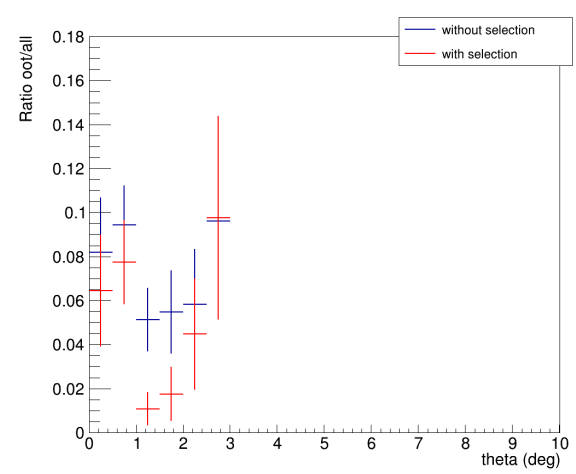

(e) Z=5

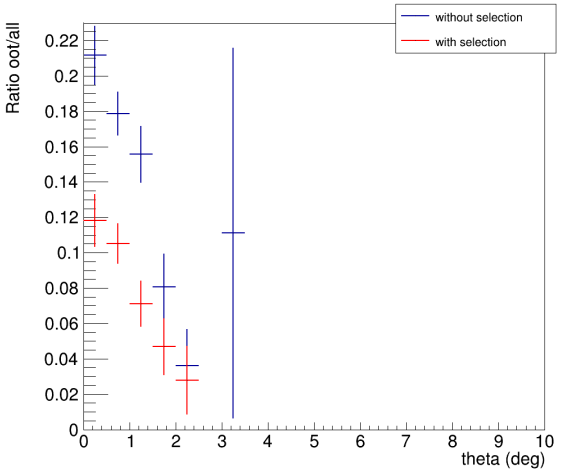

(f) Z=6

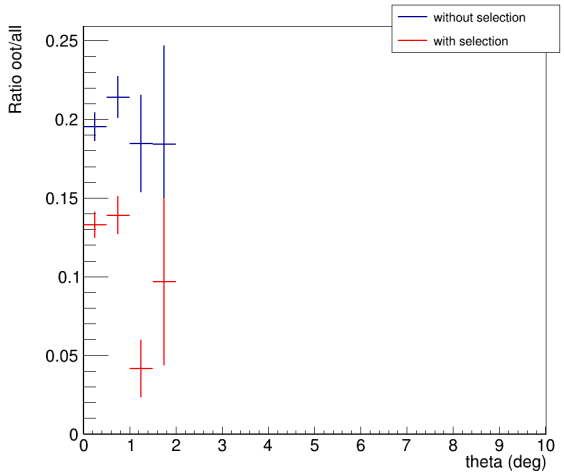

(g) Z=7

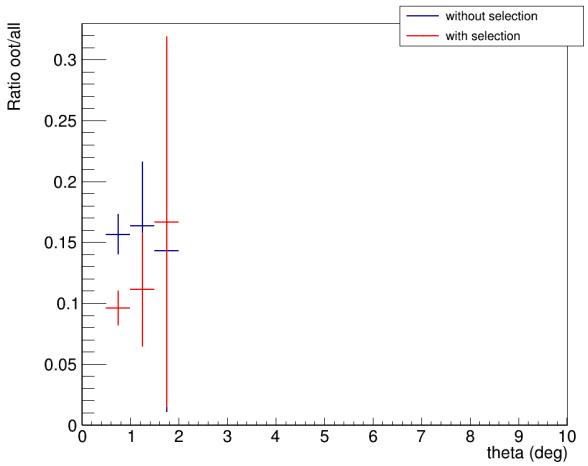

(h) Z=8

Figure 4.8: Ratio between counts of tracks originating outside the target over all tracks by angle for every charge. In blue, the reconstruction is done without selection on event type. In red, only type 1 or 2 events are selected (cont.)

Another important quantity for evaluating the selection is the ratio between the number of fragments born in the target divided by the number of all MC fragments. In Fig 4.9 it is plotted as a function of charge. It can be seen that the selection, as expected, reduces this ratio by quite a large margin. This is because the selection rejects also a non negligible amount of good events. Nevertheless, the ratio remains over 70% for fragments with $Z \geq 3$ which are the focus of the FOOT electronic setup.

On the other hand, the selection should improve the purity of the reconstruction, and this can be seen by plotting the ratio of out-of-target reconstructed fragments over the number of MC fragments of type 1 or 2, as done in Fig. 4.10. What emerges is that the selection indeed reduces considerably this ratio for all charges, which means that the selection improves the precision of track reconstruction.

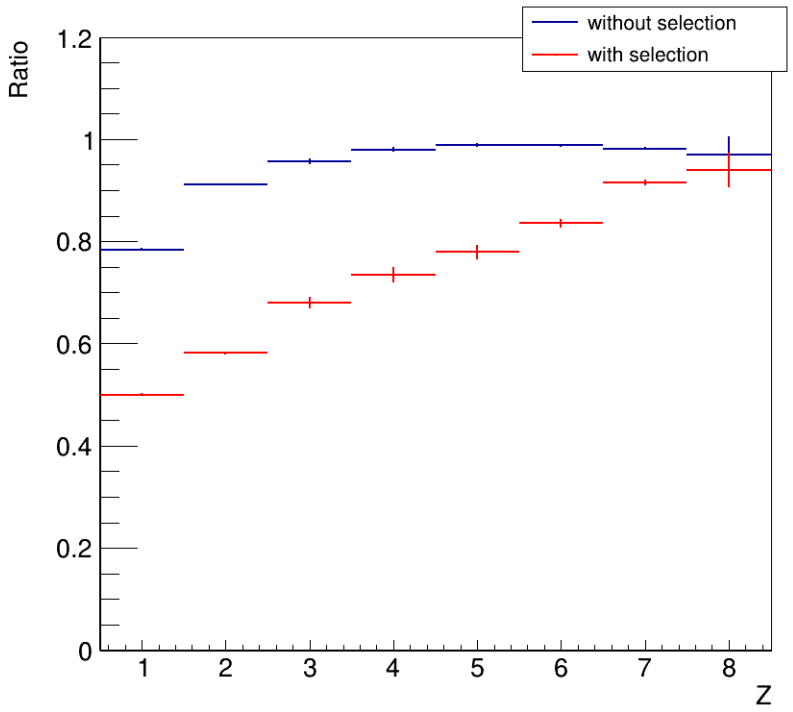

Figure 4.9: Ratio of fragments born of target fragmentation over all MC particles as a function of charge. In blue, the reconstruction is done without selection on event type. In red, only type 1 or 2 events are selected.

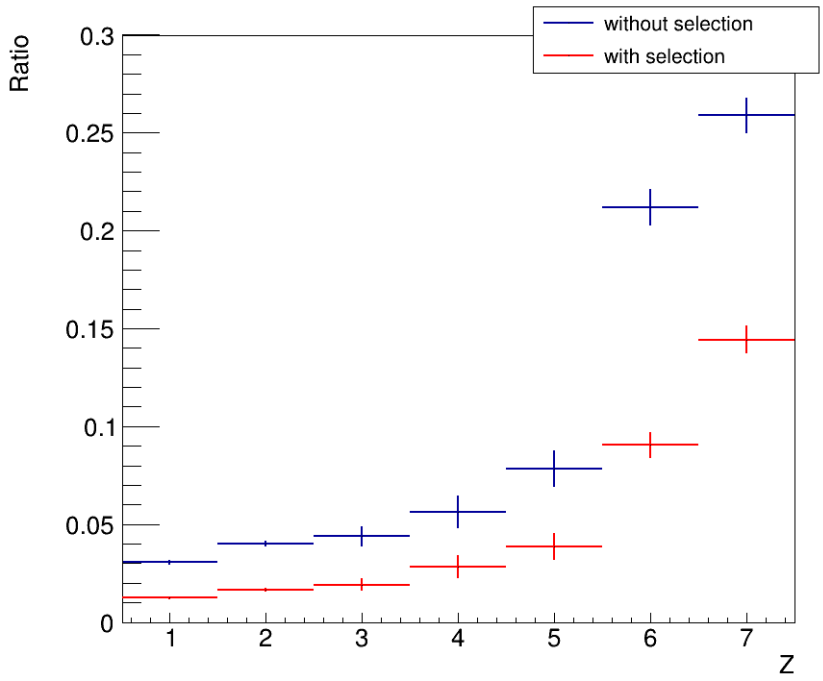

Figure 4.10: Ratio of fragments born out-of-target over MC true particles of type 1 or 2 as a function of charge. In blue, the reconstruction is done without selection on event type. In red, only type 1 or 2 events are selected.

Conclusions

The FOOT experiment has been designed with the main purpose of measuring the fragmentation cross section of light fragments (Z<10) in the energy range between 100 MeV/n and 400 MeV/n, typical for hadrontherapy applications. To do so, FOOT utilizes targets made of graphite (C) and polyethylene (C_2H_4), and a series of different detectors to track and identify the target fragments. However, there is a possibility for particles to undergo fragmentation outside the target, for example in the detectors' layers or in the air between them. These events could spoil the cross section measurements, so they should be removed from the analysis. The goal of this thesis is to study the effects of a straightforward selection of the events, obtained from a classification algorithm. This is done for a beam of ^{16}O at 400 MeV/n impinging on a target of graphite, using Monte Carlo simulated data from the experimental campaign at GSI in 2021.

First, the classification algorithm is applied to events using reconstructed information, in particular the number of hits on each layer of every detector. The accuracy of the algorithm is checked using the truth from the MC simulation, where a similar algorithm is applied. The algorithm is shown to correctly classify the vast majority of good events. However it seems that it tends to misidentify fragmentation in air for events where some fragments are lost during the flight. Furthermore, a non negligible number of reconstructed events with no hit on the ToF Wall, which are rejected from the selection, are actually good events for cross section measurements. Further studies are necessary to improve the shortcomings of the classification algorithm. A starting point would be to investigate and, in case, optimize the clusterization algorithms of both the MSD and the Tof Wall.

Afterwards, the global reconstruction analysis is performed, with and without the selection on event type to compare the results in counts of fragments, as a function of charge. The main quantity analyzed to evaluate the effectiveness of the selection is the ratio between the number of fragments originating from out-of-target interactions and the total number of reconstructed fragments. The selection vastly reduces this ratio for all charges.

Another important quantity is the ratio between as the number of reconstructed fragments that have originated in the target and the total number of MC fragments. This efficiency is obviously reduced after the selection on event type, but it stays over

70% for $Z \geq 3$, charges that the FOOT electronic setup is focused on reconstruction. A higher ratio could be obtained by improving the classification algorithm, so that it would not misidentify good events for bad events. Finally, the selection improves the purity of the reconstructed tracks, since it reduces significantly the ratio between the out-of-target reconstructed fragments and the total number of MC particles that have not re-fragmented.

In conclusion, this study demonstrates that a straightforward algorithm for event classification is generally effective in classifying events according to the zone where fragmentation happens. A selection on only good events can be used to reduce the number of out-of-target fragmentation events in the analysis, leading to a refinement of cross section measurement. This study is not a complete and final analysis of the out-of-target topic in the FOOT experiment due to the limited amount of time available, but it is a good starting point for further studies aiming to improve the event classification and selection.

Bibliography

[1] W.R. Leo. *Techniques for Nuclear and Particle Physics Experiments: A How-to Approach*. Springer, 1994.

[2] John Douglas Cockcroft. Experimental nuclear physics. *Nature*, 175, 1955.

[3] R. L. Workman et al. Review of Particle Physics. *PTEP*, 2022:083C01, 2022. doi: 10.1093/ptep/ptac097.

[4] L.E. Porter. The Barkas-effect correction to Bethe–Bloch stopping power. In *Theory of the Interaction of Swift Ions with Matter. Part 2*, volume 46 of *Advances in Quantum Chemistry*, pages 91–119. Academic Press, 2004.

[5] Robert R Wilson. Range, straggling, and multiple scattering of fast protons. *Physical review*, 71(6):385, 1947.

[6] J Hüfner, K Schäfer, and B Schürmann. Abrasion-ablation in reactions between relativistic heavy ions. *Physical Review C*, 12(6):1888, 1975.

[7] K Gunzert-Marx, H Iwase, D Schardt, and RS Simon. Secondary beam fragments produced by 200 MeV u^{-1} ^{12}C ions in water and their dose contributions in carbon ion radiotherapy. *New journal of physics*, 10(7):075003, 2008.

[8] C.A. Bertulani and P. Danielewicz. *Introduction to Nuclear Reactions*. Graduate Student Series in Physics. Taylor & Francis, 2004. ISBN 9780750309325.

[9] HL Bradt and B Peters. The heavy nuclei of the primary cosmic radiation. *Physical Review*, 77(1):54, 1950.

[10] Robert R. Wilson. Radiological use of fast protons. *Radiology*, 47(5):487–491, 1946.

[11] CA Tobias, JH Lawrence, JL Born, RK McCombs, JE Roberts, HO Anger, BVA Low-Beer, and CB Huggins. Pituitary irradiation with high-energy proton beams a preliminary report. *Cancer research*, 18(2):121–134, 1958.

[12] Particle Therapy Co-Operative Group facilities. https://www.ptcog.ch/index.php/facilities-in-operation, 2022.

[13] CNAO, Centro Nazionale di Adroterapia Oncologica. https://fondazionecnao.it/, 2023.

[14] Centro di Protonterapia, Trento. https://protonterapia.provincia.tn.it/, 2023.

[15] CATANA, Centro di AdroTerapia ed Applicazioni Nucleari Avanzate. https://www.lns.infn.it/it/applicazioni/catana.html, 2023.

[16] Solange Gagnebin. *Experimental determination of absorbed dose to water in a scanned proton beam using a water calorimeter and an ionization chamber*. PhD thesis, University of Alberta, Canada, 05 2010.

[17] David Jette and Weimin Chen. Creating a spread-out Bragg peak in proton beams. *Physics in Medicine & Biology*, 56(11):N131, 2011.

[18] Takeichiro Yokoi, John Cobb, Ken Peach, Gemma Morgan, Juergen Pozimski, and Matthew Easton. Beam injection issues of ffag for particle therapy. 06 2008.

[19] Andrew E Ekpenyong. *Mathematical Physics for Nuclear Experiments*. CRC Press, 2022.

[20] Sayyed Bijan Jia, Ali Asghar Mowlavi, MH Hadizadeh, and M Ebrahimi Loushab. Impact of range straggling and multiple scattering on proton therapy of brain, using a slab head phantom. *International Journal of Radiation Research*, 12(2):171, 2014.

[21] Sandro Rossi. Hadron therapy achievements and challenges: The CNAO experience. *Physics*, 4(1):229–257, 2022. ISSN 2624-8174.

[22] Giuseppe Battistoni, I Mattei, and S Muraro. Nuclear physics and particle therapy. *Advances in Physics: X*, 1(4):661–686, 2016.

[23] Atsushi Ito, Hisako Nakano, Yohsuke Kusano, Ryoichi Hirayama, Yoshiya Furusawa, Chieko Murayama, Tomoyuki Mori, Yosuke Katsumura, and Kunio Shinohara. Contribution of indirect action to radiation-induced mammalian cell inactivation: dependence on photon energy and heavy-ion LET. *Radiation research*, 165(6):703–712, 2006.

[24] Ute Linz. Physical and biological rationale for using ions in therapy. *Ion Beam Therapy: Fundamentals, Technology, Clinical Applications*, pages 45–59, 2012.

[25] Yoshiya Furusawa. Heavy-ion radiobiology. *Carbon-ion radiotherapy: Principles, practices, and treatment planning*, pages 25–37, 2014.

[26] Amin Kassis. Therapeutic radionuclides: Biophysical and radiobiologic principles. *Seminars in nuclear medicine*, 38:358–66, 10 2008. doi: 10.1053/j.semnuclmed.2008.05.002.

[27] Johan Martin Søbstad. Monte Carlo based comparison of constant vs. variable RBE for proton therapy patients. 2017.

[28] Tatiana Wenzl and Jan J Wilkens. Modelling of the oxygen enhancement ratio for ion beam radiation therapy. *Physics in Medicine & Biology*, 56(11):3251, 2011.

[29] J Dudouet, D Juliani, M Labalme, D Cussol, JC Angélique, B Braunn, J Colin, Ch Finck, JM Fontbonne, H Guérin, et al. Double-differential fragmentation cross-section measurements of 95 MeV/nucleon ^{12} C beams on thin targets for hadron therapy. *Physical Review C*, 88(2):024606, 2013.

[30] Giuseppe Battistoni, Marco Toppi, and Vincenzo Patera. Measuring the impact of nuclear interaction in particle therapy and in radio protection in space: the FOOT experiment. *Frontiers in Physics*, 8:568242, 2021.

[31] Giuliana Galati, Andrey Alexandrov, Behcet Alpat, Giovanni Ambrosi, Stefano Argirò, Raul Arteche Diaz, Nazar Bartosik, Giuseppe Battistoni, Nicola Belcari, Elettra Bellinzona, et al. Charge identification of fragments with the emulsion spectrometer of the FOOT experiment. *Open Physics*, 19(1):383–394, 2021.

[32] L Galli, AM Baldini, F Cei, M Chiappini, M Francesconi, M Grassi, U Hartmann, M Meucci, F Morsani, D Nicolò, et al. WaveDAQ: An highly integrated trigger and data acquisition system. *Nuclear Instruments and Methods in Physics Research Section A: Accelerators, Spectrometers, Detectors and Associated Equipment*, 936: 399–400, 2019.

[33] Yunsheng Dong, Silvestre Gianluigi, Colombi Sofia, Alexandrov Andrey, Alpat Behcet, Ambrosi Giovanni, Argirò Stefano, Raul Arteche Diaz, Barbanera Mattia, Bartosik Nazar, et al. The drift chamber detector of the FOOT experiment: Performance analysis and external calibration. *Nuclear Instruments and Methods in Physics Research Section A: Accelerators, Spectrometers, Detectors and Associated Equipment*, 986:164756, 2021.

[34] E Spiriti, Ch Finck, J Baudot, C Divay, D Juliani, M Labalme, M Rousseau, S Salvador, M Vanstalle, C Agodi, et al. CMOS active pixel sensors response to low energy light ions. *Nuclear Instruments and Methods in Physics Research Section A: Accelerators, Spectrometers, Detectors and Associated Equipment*, 875:35–40, 2017.

[35] AC Kraan, R Zarrella, A Alexandrov, B Alpat, G Ambrosi, S Argirò, R Arteche Diaz, N Bartosik, G Battistoni, N Belcari, et al. Charge identification of nuclear fragments with the FOOT Time-Of-Flight system. *Nuclear Instruments and Methods in Physics Research Section A: Accelerators, Spectrometers, Detectors and Associated Equipment*, 1001:165206, 2021.

[36] GSI accelerators. `https://www.gsi.de/en/researchaccelerators/accelerator_facility`, 2023.

[37] R. Brun and F. Rademakers. ROOT: An object oriented data analysis framework. *Nucl. Instrum. Meth. A*, 389:81–86, 1997. doi: 10.1016/S0168-9002(97)00048-X.

[38] SHOE repository. `https://baltig.infn.it/asarti/shoe`, 2023.

[39] Giuseppe Battistoni, Julia Bauer, Till T Boehlen, Francesco Cerutti, Mary PW Chin, Ricardo Dos Santos Augusto, Alfredo Ferrari, Pablo G Ortega, Wioletta Kozłowska, Giuseppe Magro, et al. The FLUKA code: an accurate simulation tool for particle therapy. *Frontiers in oncology*, 6:116, 2016.

[40] Johannes Rauch and Tobias Schlüter. GENFIT—a generic track-fitting toolkit. In *Journal of Physics: Conference Series*, volume 608, page 012042. IOP Publishing, 2015.

[41] SHOE reconstruction software. `http://arpg-serv.ing2.uniroma1.it/twiki/bin/view/Main/FOOTReconstruction`, 2023.

[42] Riccardo Ridolfi. The FOOT experiment: Trigger and data acquisition (TDAQ) development and data analysis. 2022.

[43] Rudolf Frühwirth. Application of Kalman filtering to track and vertex fitting. *Nuclear Instruments and Methods in Physics Research Section A: Accelerators, Spectrometers, Detectors and Associated Equipment*, 262(2-3):444–450, 1987.

[44] Kaltest: A ROOT-based Kalman Filter package. `https://www-jlc.kek.jp/subg/offl/kaltest/`, 2023.

[45] Giacomo Ubaldi. Analysis of fragmentation cross sections of GSI 2021 data for the FOOT experiment, 2022. Master's Thesis.